Journal of Alloys and Compounds 879 (2021) 160464

Contents lists available at ScienceDirect

Journal of Alloys and Compounds

journal homepage: www.elsevier.com/locate/jalcom

Corrosion resistance of crystalline and amorphous CuZr alloys in NaCl aqueous environment and effect of corrosion inhibitors

Chenyang Xie[a,b], Ingrid Milošev[c], Frank U. Renner[b], Anton Kokalj[c], Pere Bruna[a], Daniel Crespo[a,*]

[a] Department of Physics, INTE & Barcelona Multiscale Res. Center, Universitat Politècnica de Catalunya, Barcelona, Catalunya, Spain
[b] Institute for Materials Research (IMO) & IMOMEC, Hasselt University, Diepenbeek, Belgium
[c] Jožef Stefan Institute, Department of Physical and Organic Chemistry, Ljubljana, Slovenia

ARTICLE INFO

Article history:
Received 16 September 2020
Received in revised form 14 May 2021
Accepted 16 May 2021
Available online 19 May 2021

Keywords:
CuZr
Crystalline alloys
Amorphous alloys
Corrosion inhibition
Imidazole-based inhibitors

ABSTRACT

CuZr alloys are the basis of a family of metallic glasses with large glass forming ability and remarkable mechanical properties. The corrosion response of prepared crystalline and amorphous Cu_xZr_{100-x} alloys (x = 40, 50, 64 at%), as well as bare Cu and Zr, in a severe corrosive environment, was tested. The alloys were immersed in 3 wt% NaCl aqueous solution. With the aim to increase the resistance of copper as less corrosion alloy component, nine imidazole-based compounds with different functional groups were tested as potential corrosion inhibitors. Potentiodynamic polarization measurements, electrochemical impedance spectroscopy, and long-term immersion tests followed by X-ray photoelectron spectroscopy and microscopy analysis were carried out. Overall, all the tested amorphous alloys exhibit a much better corrosion resistance than their crystalline counterparts in the presence and absence of inhibitors. The main factor controlling the corrosion resistance of the alloys appears to be the Zr-rich (or at least equiatomic) amorphous structure, the effect of the inhibitors being secondary. Results therefore show a complex relationship between inhibitor performance, microstructure and composition of CuZr alloys.

1. Introduction

CuZr alloys are the basis of one of the most widely studied families of metallic glasses (MG) [1–4] and have become a *de facto* archetypical MG. From early work, it is known that $Cu_{100-x}Zr_x$ (at%) metallic glasses can be obtained by melt-spinning in a wide composition range of x = 25–60 [5]. Potential industrial applications taking advantage of their interesting mechanical properties [6,7] require also to assess their chemical stability. MG surfaces are smooth and free of voids, dislocations and/or atomic terraces, which are features that often contribute to improved corrosion resistance. The amorphous CuZr system is an excellent glass former, and although the amorphous surfaces are wavy and irregular, they show large chemical homogeneity and improved corrosion resistance [8–14].

Beyond the intrinsic interest of CuZr metallic glasses, it must be noted that copper is used in a vast number of industrial applications [15]. For this reason, several approaches have been used to control, inhibit and eventually suppress corrosion in copper. Between them, corrosion control in aqueous solution has been attempted by adding both inorganic and organic inhibitors. Organic inhibitors show, in general, a better performance than inorganic ones [16]. Among them, azole compounds are known for their ability to inhibit the corrosion on Cu based materials [17,18], with benzotriazole being a notable example that has been widely used [19]. Mercapto based azoles are also promising [20,21], but the search of less toxic and effective alternatives is still an active research subject. Zirconium metal has much less industrial importance than Cu, although it is essential in the nuclear industry. It is a very reactive metal, prone to fast oxidation. Zirconium oxide is an important component of fine ceramics.

Comparison of the properties of crystalline and amorphous alloys of the same composition is a very interesting way to understand the effects of topology on their macroscopic properties [22]. The comparison of the corrosion mechanisms of crystalline and amorphous alloys of the same stoichiometry would give valuable data regarding the effect of crystalline structure on the corrosion performance. A

* Corresponding author.
E-mail addresses: chenyang_xie@hotmail.com (C. Xie), ingrid.milosev@ijs.si (I. Milošev), frank.renner@uhasselt.be (F.U. Renner), tone.kokalj@ijs.si (A. Kokalj), pere.bruna@upc.edu (P. Bruna), Daniel.Crespo@upc.eduu (D. Crespo).

https://doi.org/10.1016/j.jallcom.2021.160464
0925-8388/

number of literature studies are available discussing the properties and corrosion mechanisms of CuZr-based metallic glasses [11,23–26]. Although many CuZr based alloys show good corrosion resistance, such as $Zr_{55}Cu_{20}Ni_{10}Al_{10}Ta_5$ (at%), $Zr_{50}Cu_{20}Ni_{10}Al_{10}Ta_{10}$ (at %) or $Zr_{55}Cu_{20}Ni_{10}Al_{10}Ti_5$ (at%), the parent CuZr alloy is not particularly corrosion resistant. The observed differences in corrosion resistance may be attributed mostly to the different surface crystalline structure, i.e. the ordered – probably polycrystalline – atomic structure in the crystal vs. the disordered but chemically homogeneous atomic distribution in amorphous alloys [27,28]. This is one argument to choose a binary alloy; the comparison of corrosion resistant multicomponent alloys with their crystalline counterparts has much less significance as the role of the minor elements would be undiscernible. It has also been noted that an additional source of protection against corrosion in amorphous materials might be the development of amorphous oxide layers; the absence of grain boundaries in these oxide layers may reduce the ion mobility [23].

The different chemistry of Cu and Zr makes one assume that corrosion inhibitors that are beneficial for one of the metals may not have a similar effect for the other. We are dealing with alloys of two different metals with Cu being more susceptible to corrosion, therefore we address herein the potential of Cu corrosion inhibitors on both crystalline and amorphous CuZr alloys. In this work, we test the utility of organic compounds consisting of imidazole, mercaptobenzimidazole and hydroxybenzimidazole derivatives as corrosion inhibitors for CuZr alloys in 0.51 M (or equivalently 3 wt%) NaCl solution; these inhibitors were chosen from a larger set of inhibitors from our previous publication [29]. Electrochemical and immersion tests were conducted in order to investigate the inhibition performance of these organic compounds on the CuZr alloys of different composition ($Cu_{40}Zr_{60}$, $Cu_{50}Zr_{50}$ and $Cu_{64}Zr_{36}$) and microstructure (crystalline and amorphous). X-ray photoelectron spectroscopy (XPS) was utilized to investigate the composition of organic layers formed on the surface of the alloys.

2. Materials and methods

2.1. Materials and chemicals

Crystalline samples for corrosion tests were produced from high purity raw materials (Cu 99.9%, Zr 99.8% excluded Hf, Hf 2% nominal, Alfa-Aesar). Samples were melted twice on an arc melter oven (Compact Arc Melter MAM-1, Edmund Bühler GmbH) provided with a water-cooled plate, on a Ti-gettered Ar (99.995% Nippon gases) atmosphere at a pressure of ~700 hPa. Circular samples were cut with a low speed diamond saw from the arc melted alloy, having a surface area of 0.5–1.0 cm^2. They were further welded on the back to a copper wire and embedded with epoxy resin. Samples were then sequentially ground with P600, P1200, P2000, P4000 SiC (CarbiMet) abrasive paper and polished with 6 µm, 3 µm and 1 µm MetaDi diamond suspensions (Buehler). Samples were then cleaned with ethanol in an ultrasonic bath for 3 min, double-rinsed with distilled water and dried with nitrogen gas.

Amorphous samples were produced with the same raw materials as crystalline. Amorphous ribbon materials of approximately 40 µm thickness and 1.5 mm in width were produced on an Edmund Bühler melt spinner in Ar (99.995%) atmosphere at 1 mm of crucible-wheel distance surface and wheel velocity of 40 ± 1 m/s. Corrosion tests for amorphous samples were performed on the free side of the ribbons which acted as the working electrode. To prepare the ribbon for measurements, it was connected to a pure copper (99.9%) strip by a PTFE tape to get an electrical connection; the copper strip and the wheel side of the ribbon were then covered by PTFE tape, see Fig. S1 in the Supplementary material.

The choice of alloy compositions was driven by good glass forming ability. The selected alloy compositions are denoted as Cu_xZr_{100-x} (x = 40, 50 and 64 at%), i.e. $Cu_{40}Zr_{60}$, $Cu_{50}Zr_{50}$ and $Cu_{64}Zr_{36}$.

Electrochemical corrosion tests were carried out in 3 wt% (0.51 M) NaCl (Panreac Quimica (p.a.)) aqueous solution with or without the addition of organic compounds tested as corrosion inhibitors. Nine compounds were tested. To facilitate the presentation they are divided in three groups:

(1) imidazole derivatives: imidazole (ImiH, 99.5%), 2-mercapto-1-methylimidazole (SH-ImiMe, 99%), 2-mercapto-4-phenylimidazole (SH-ImiH-4Ph, 97%),
(2) mercaptobenzimidazole derivatives: 2-mercaptobenzimidazole (SH-BimH, 98%), 2-mercapto-5-methoxybenzimidazole (SH-BimH-5OMe, 99%), 5-amino-2-mercaptobenzimidazole (SH-BimH-5NH_2, 96%), 2-(methylthio)benzimidazole (Me-S-BimH, 97%), and
(3) hydroxybenzimidazole derivates: 2-hydroxybenzimidazole (OH-BimH, 97%), benzimidazole-2-methanol (OH-Me-BimH, 97%.

All compounds were used at a concentration of 1 mM. Skeletal formulae of the inhibitors are presented in Fig. 1. Note that Me-S-BimH is strictly not a mercapto-compound (R–SH) because it contains sulfur bonded to methyl group (R–SCH_3) but it is nevertheless a derivative of mercaptobenzimidazole and is therefore included in this group of compounds. Benzimidazole-2-methanol was supplied by Fluorochem and other inhibitors were supplied by Sigma–Aldrich. Compounds were used as supplied.

2.2. Structural characterization

The crystalline and as-cast ribbons were examined using Bruker D8 Advance X-ray diffractometer (XRD) equipped with Cu Kα X-ray tube with radiation (λ = 1.5418 Å) in Bragg-Brentano geometry. The thermal stability of the amorphous samples was evaluated using a NETZSCH DSC 404 F3 differential scanning calorimeter (DSC) at a heating rate of 20 K/min under a flow of high purity N_2.

2.3. Electrochemical measurements

Electrochemical tests were performed in a three-electrode corrosion cell (volume 0.1 L, Bio-logic, France) at 25 °C in 3 wt% NaCl. An Ag/AgCl (3.5 M KCl) electrode (+0.205 V vs. saturated hydrogen electrode at 25 °C) was used as reference electrode and a spiral platinum wire (~3.6 cm^2) was used as a counter electrode. Specimens' surface exposed to solution was around 0.5–1.0 cm^2 for crystalline samples and around 0.05–0.2 cm^2 for amorphous ones. Measurements were carried out with a SP-200 Bio-Logic (Bio-Logic Science Instruments, France) potentiostat/galvanostat operated by the EC-Lab software. Crystalline samples were polished before every measurement, while all measurements on amorphous samples were performed on fresh ribbons (*Section* 2.1.).

2.3.1. Potentiodynamic measurements

The specimens were stabilized under open circuit condition for 1 h before the measurements. During that time, the open circuit potential was measured as a function of time. The stable, quasi-steady state potential reached at the end of the stabilization period is denoted the open circuit potential (OCP). Potentiodynamic polarization curves were recorded starting at 250 mV negative to OCP, then increasing the potential in the anodic direction at a potential scan rate of 1 mV/s. A maximum positive potential of 650 mV, relative to OCP, was applied to crystalline samples, and of 250 mV for

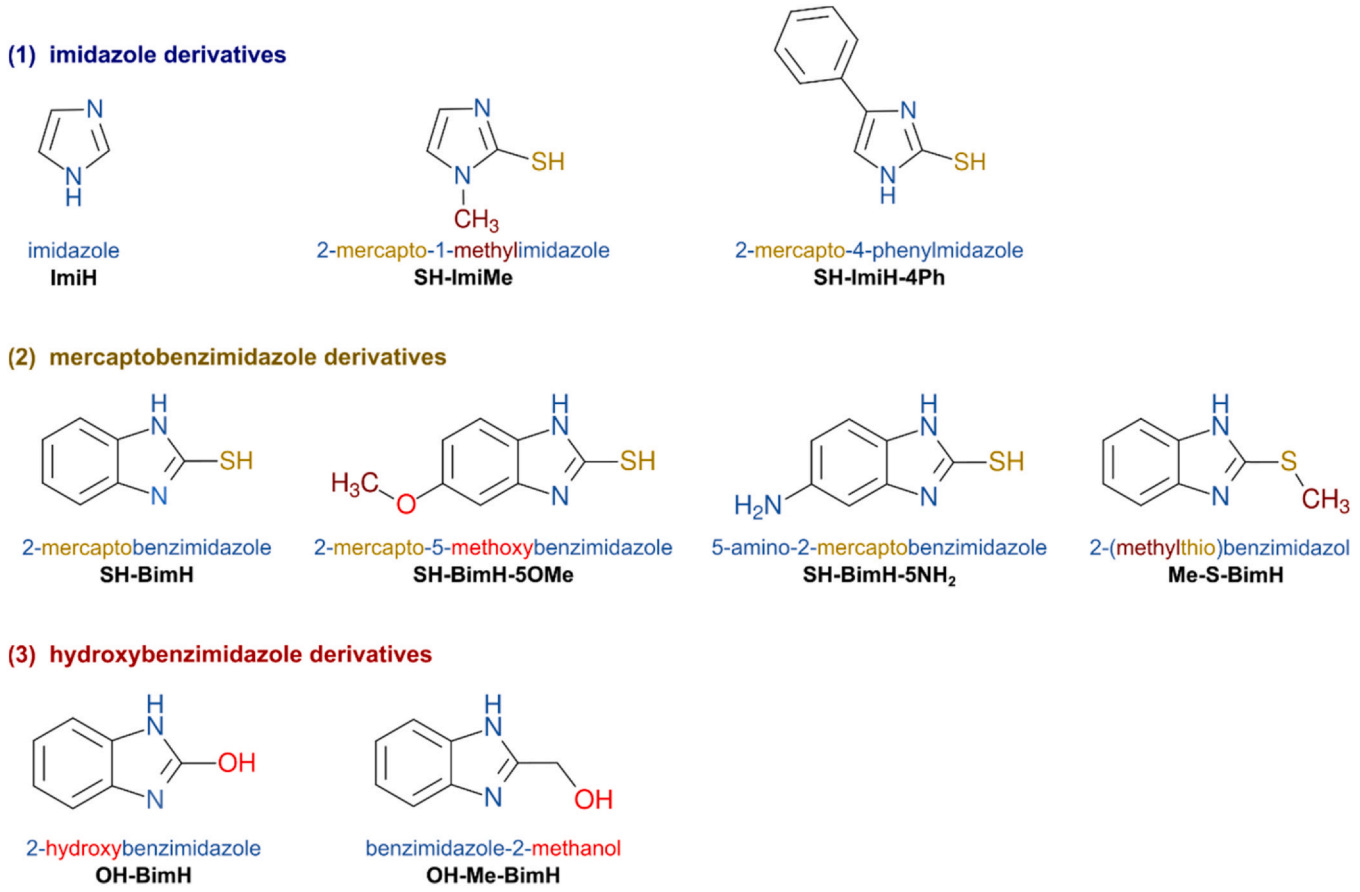

Fig. 1. Skeletal formulae of the organic molecules and their shorthand labels, tested as corrosion inhibitors in this work, and their classification into three groups: (1) imidazole derivatives, (2) mercaptobenzimidazole derivatives, and (3) hydroxybenzimidazole derivatives.

amorphous ones due to the smaller thickness of the ribbon. All the measurements were performed at least twice, and the typical standard deviation is below 12%.

2.3.2. Electrochemical impedance spectroscopy

Electrochemical impedance spectroscopy (EIS) measurements were performed at open circuit conditions in the frequency range from 10^5 Hz to 10^{-2} Hz. AC excitation voltage was 10 mV (rms). EIS spectra were recorded after 1 h at the OCP and up to 120 h immersion in periods of 24 h. The modulus of impedance $|Z|$ at frequency of 10^{-2} Hz was taken as a significant parameter of the corrosion resistance of the metal covered by an inhibitor layer. The typical standard deviation of the measurements is around 15%, and in all cases below 30%.

2.4. Immersion Tests

Immersion tests were carried out in a sealed polyethylene container with an electrolyte volume/sample surface ratio larger than 25 mL/cm^2. Amorphous alloys $Cu_{50}Zr_{50}$ and $Cu_{64}Zr_{36}$ were immersed for 5 days and $Cu_{40}Zr_{60}$ for 12 days due to its good corrosion resistance. All crystalline alloys were immersed for 5 days.

2.5. Surface characterization

The samples were analyzed using a scanning electron microscope (SEM) at electron beam energy of 15 keV at a Neon40 Crossbeam™ workstation in a back scattered electron mode. Prior to analysis, the surface was coated by a thin carbon layer to reduce charging.

X-ray photoelectron spectroscopy (XPS) was performed with a SPECS system equipped with a Phoibos 150 MCD-9 detector and an Al anode XR50 source operating at 150 W. Scan step for high-resolution analysis is 0.1 eV. The diameter of the analyzed spot was 1 mm^2. CasaXPS program (Casa Software Ltd., UK) was used to evaluate the XPS data. The spectra were normalized on the binding energy scale relative to the position of C 1s peak at 284.8 eV. When calculating the chemical composition, the intensity of carbon signal was not taken into consideration. The spectra were not normalized on the intensity scale.

3. Results

3.1. Characterization of as prepared alloys

As prepared amorphous and crystalline CuZr alloys were first characterized by X-ray diffraction (XRD), differential scanning calorimetry (DCS) and X-ray photoelectron spectroscopy (XPS) to reveal their structure, phase transition properties and composition.

XRD patterns of the as-cast melt-spun amorphous samples with different Cu/Zr ratio are shown in Fig. 2a. Three melt-spun alloys are amorphous as indicated by a typical broad amorphous peak and the absence of any detectable crystalline peaks. Fig. 2b shows the DSC curves of the amorphous CuZr alloys. This termoanalytical technique serves to determine crystallization and glass transition events (T_x and T_g). Both T_x and T_g increase with the Cu content. The

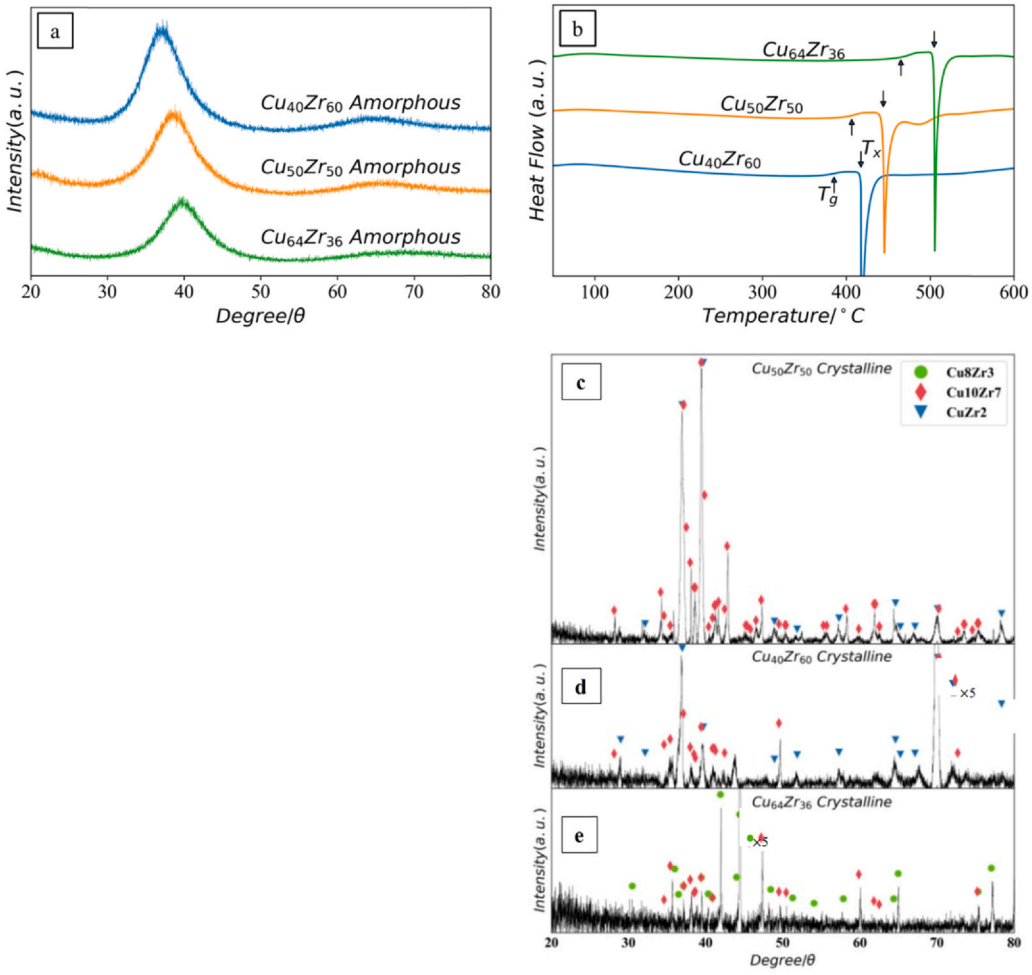

Fig. 2. (a) X-ray diffraction (XRD) spectra, (b) differential scanning calorimetry (DSC) curves of amorphous CuZr alloys and XRD spectra of (c) $Cu_{40}Zr_{60}$, (d) $Cu_{50}Zr_{50}$ and (e) $Cu_{64}Zr_{36}$ crystalline alloys.

temperature range of the supercooled liquid ($\Delta T = T_x - T_g$) is a signature of the glass-forming ability of the alloys, and it is similar in all compositions.

XRD patterns of the as-cast crystalline samples with different Cu/Zr ratio are shown in Fig. 2c–e. The main crystalline phase in $Cu_{40}Zr_{60}$ is identified to be $CuZr_2$, although it may also contain traces of $Cu_{10}Zr_7$. $Cu_{50}Zr_{50}$ is composed of $CuZr_2$ and $Cu_{10}Zr_7$, while $Cu_{10}Zr_7$ and Cu_8Zr_3 are identified in $Cu_{64}Zr_{36}$. All the identified phases are coherent with the phase diagram [30] provided in the Supplementary material Fig. S2.

High energy resolution XPS spectra recorded for as-prepared amorphous and crystalline CuZr alloys are presented in Figs. 3 and 4. The surface consists of Cu, Zr and O; the chemical compositions deduced from XPS spectra are given in Tables 1 and 2. For Cu, both Cu 2p and LMM spectra are presented as to be able to differentiate between Cu and Cu(I) species, which is not possible with Cu 2p spectra alone [20,31]. The surface concentration of Cu in $Cu_{40}Zr_{60}$ and $Cu_{50}Zr_{50}$ amorphous alloys (Fig. 3) is negligible and the surface predominantly consists of ZrO_2 oxide [31]. This layer is few nanometers thick and allows the detection of Zr and suboxide peaks [32,33] originating from the underlying alloy substrate. The Zr/O ratio is smaller than the stoichiometric ratio of 0.5 (Table 1) which may be attributed to exposure of the sample to air, as suggested by the position of O 1s peak center in the hydrated region (OH^- and H_2O peaks). In Fig. 3c, Zr/Zr suboxide peaks exist and ZrO_2 peaks are strong; as shown in the reference, thin ZrO_2 native oxide film with thickness of several nanometers is always present and below it are Zr and Zr suboxide. The spectra of $Cu_{64}Zr_{36}$ alloy, however, show different composition: copper can be now detected at 1.3 at% (note that for the former two alloys the spectra are given but not commented due to their low intensities). The Cu 2p spectrum proves that the surface consists of Cu and/or Cu_2O since there is no satellite peak, which would indicate the presence of CuO [20]. The Cu LMM spectra, however, corroborate the presence of Cu and small amount of Cu_2O (Cu is probably originating from underlying substrate. The Cu/Zr ratio is 0.06 reflecting a complete predominance of a uniform ZrO_2 in the surface layer formed on amorphous CuZr alloys regardless of their composition.

CuZr crystalline alloys show higher Cu content than CuZr amorphous alloys (Fig. 4 and Table 2). The crystalline structures caused different oxidation behavior than for amorphous alloys, where uniform ZrO_2 surface layer was formed. For crystalline alloys, the surface layers contain both Cu and Zr (Fig. 4). Cu_2O oxide is the major Cu compound on the crystalline surface, as evident in Cu LMM spectra where the Cu_2O completely prevails over that of Cu, in contrast to amorphous alloys (Fig. 3). In Zr 3d spectra, the ZrO_2 is the only peak and no peak related to Zr/Zr suboxide appears. Note that the Cu/Zr ratios are smaller than the stoichiometric ratios of 0.67, 1 and 1.7[1] (Table 2) still reflecting that also in crystalline alloys Zr oxide remains a predominant surface oxide; however, the portion of Cu

[1] Note that the surface was air-exposed and in order to obtain the composition of bulk alloy one should sputter-cleaned the surface.

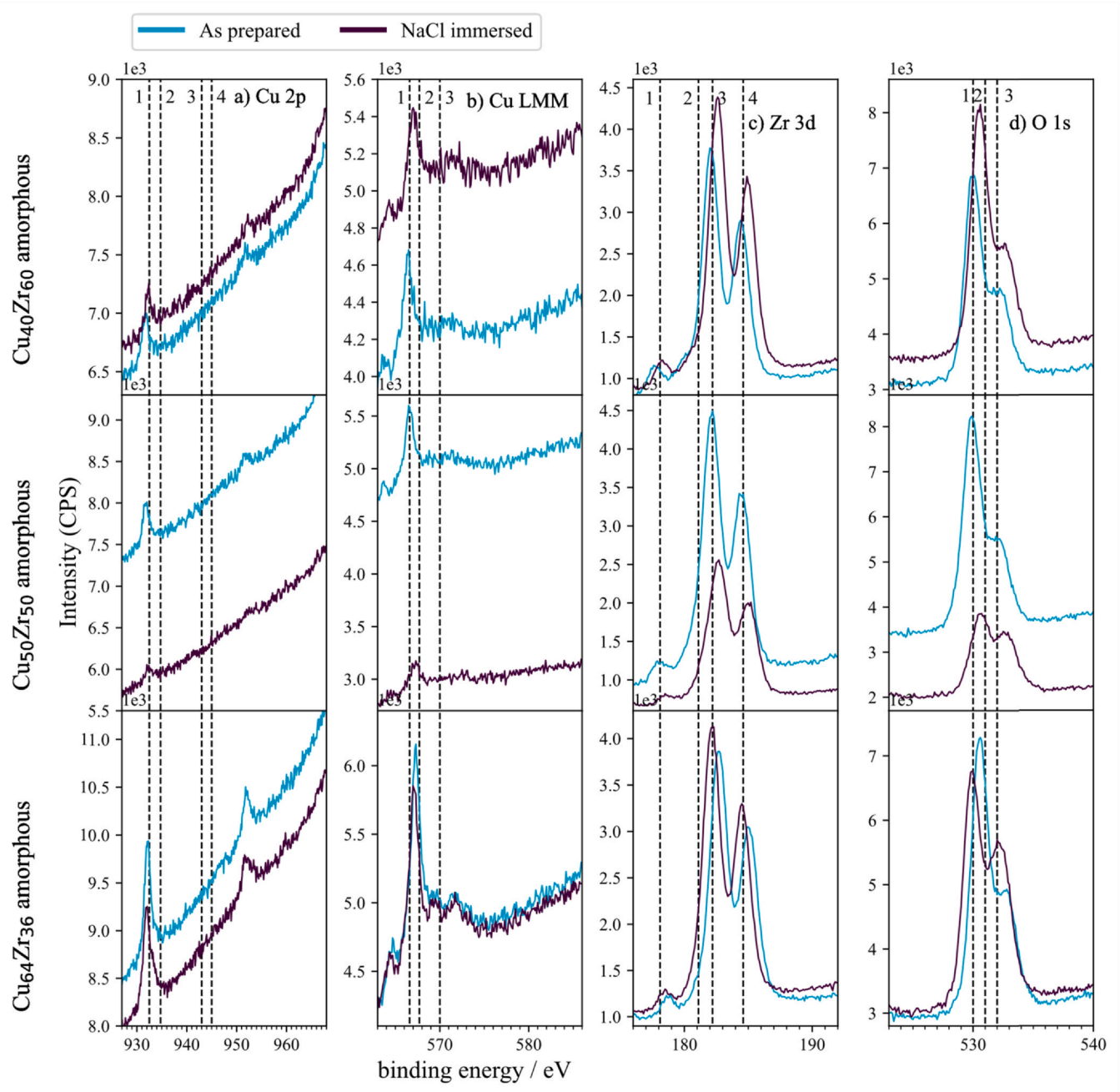

Fig. 3. High-resolution XPS (a) Cu 2p, (b) Cu LMM, (c) Zr 3d and (d) O 1s spectra of the surface of as-prepared amorphous alloys and immersed for 24 h in 3 wt% NaCl solution (blank). Top: $Cu_{40}Zr_{60}$, center: $Cu_{50}Zr_{50}$, bottom: $Cu_{64}Zr_{36}$. Dash lines represent the position of peaks of reference compounds: (a) 1: Cu/Cu_2O, 2: $CuO/Cu(OH)_2$, 3: Cu(II) satellite peak, (b) 1: Cu, 2: CuO, 3: Cu_2O, (c) 1, 2: Zr/Zr sub-oxide, 3, 4: ZrO_2, (d) 1: O^{2-}, 2: OH^-, 3: H_2O. Note that the spectra were not normalized on the intensity scale.

oxide is much larger than in the case of amorphous alloys (Table 1). The Zr/O ratio is somewhat smaller than for amorphous alloys (Tables 1 and 2) but the position of O 1s peak center is predominantly in the oxide/hydroxide region (O^{2-} and OH^- peaks). These spectra indicate that the surface layers formed on crystalline alloys differ from those on amorphous alloys not only in composition but also in thickness: the layers are richer in copper and thicker.

3.2. Characterization of Cu and Zr metals and CuZr alloys in NaCl solution

Fig. 5 schematically shows the interface structure between electrode and electrolyte, based on the model postulated by Xu et al. [31]. The native oxide passive layer of the CuZr amorphous alloys turns out to be ZrO_2 oxide, developed over a Cu-rich region above the amorphous matrix. The thickness of the ZrO_2 layer increases with the concentration of Zr and the formation of Cu-rich region is caused by the diffusion of Zr to the surface. This model is exactly corroborated by our XPS data (Figs. 3 and 4).

Due to the ultrafast initial oxidation process, the ZrO_2 ultrathin passive film becomes the interface between sample surface and electrolyte. Additionally, ZrO_2 has a large dielectric constant, 10–23, and huge resistivity, 3.16×10^5 to 3.16×10^{10} Ω m, which provides protection for the material in a corrosive electrolyte. Introduction of inhibitors in the electrolyte is expected to induce a rapid physisorption and may result in eventual chemisorption on the surface.

The spontaneously formed dielectric film is inhomogeneous, as indicated in Fig. 5a. This anodic oxide layer is well described by

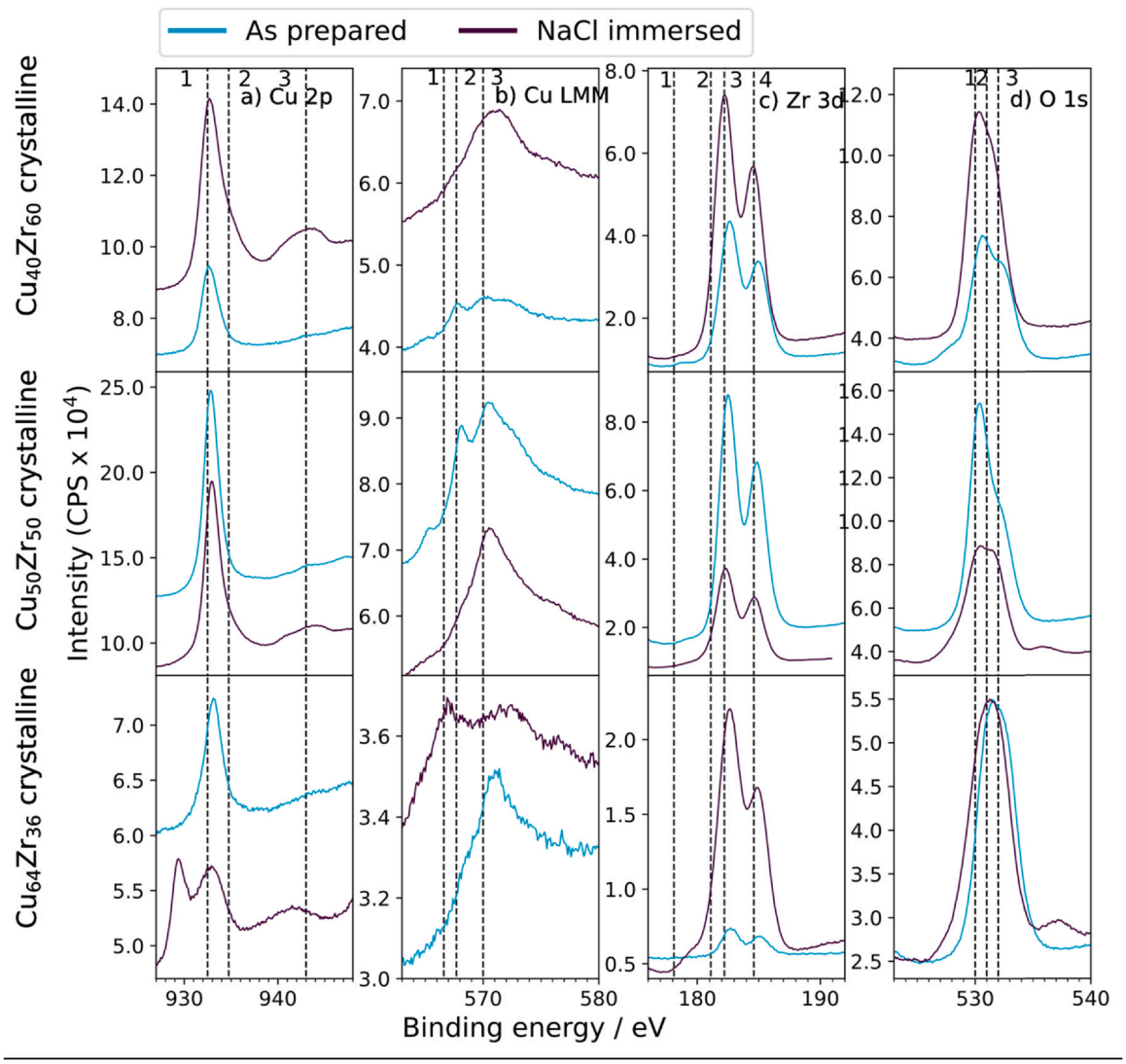

Fig. 4. High-resolution XPS (a) Cu 2p, (b) Cu LMM, (c) Zr 3d and (d) O 1s spectra of the surface of as-prepared crystalline alloys and immersed for 24 h in 3 wt% NaCl solution (blank). Top: $Cu_{40}Zr_{60}$, center: $Cu_{50}Zr_{50}$, bottom: $Cu_{64}Zr_{36}$. Dash lines represent the position of peaks of reference compounds: (a) 1: Cu/Cu_2O, 2: $CuO/Cu(OH)_2$, 3: Cu(II) satellite peak, (b) 1: Cu, 2: CuO, 3: Cu_2O, (c) 1, 2: Zr/Zr sub-oxide, 3, 4: ZrO_2, (d) 1: O^{2-}, 2: OH^-, 3: H_2O. Note that the spectra were not normalized on the intensity scale.

Table 1
Concentration of Cu, Zr and O calculated from Cu 2p, Zr 3d and O 1s XPS spectra (Fig. 3) recorded on the surface of as-prepared CuZr amorphous alloys and after 24 h immersion in 3 wt% NaCl.

Sample	Composition (at%)			Ratio	
	Cu	Zr	O	Cu/Zr	Zr/O
As-prepared amorphous alloys					
$Cu_{40}Zr_{60}$	< 0.1	26.8	73.1	–	0.37
$Cu_{50}Zr_{50}$	< 0.1	21.4	78.5	–	0.27
$Cu_{64}Zr_{36}$	1.3	20.7	78.0	0.06	0.26
Amorphous alloys after immersion in NaCl					
$Cu_{40}Zr_{60}$	< 0.1	20.5	79.4	–	0.26
$Cu_{50}Zr_{50}$	< 0.1	26.4	73.5	–	0.36
$Cu_{64}Zr_{36}$	1.1	16.7	82.2	0.06	0.20

Table 2
Concentration of Cu, Zr and O calculated from Cu 2p, Zr 3d and O 1s XPS spectra (Fig. 4) recorded on the surface of as-prepared CuZr crystalline alloys and after 24 h immersion in 3 wt% NaCl. Note that due to technical reasons the data for $Cu_{64}Zr_{36}$ could not be elaborated.

Sample	Composition (at%)			Ratio	
	Cu	Zr	O	Cu/Zr	Zr/O
As-prepared crystalline alloys					
$Cu_{40}Zr_{60}$	1.5	16.9	81.6	0.09	0.21
$Cu_{50}Zr_{50}$	4.2	18.0	77.8	0.23	0.23
$Cu_{64}Zr_{36}$	\	\	\	\	\
Crystalline alloys after immersion in NaCl					
$Cu_{40}Zr_{60}$	2.9	19.0	78.1	0.15	0.24
$Cu_{50}Zr_{50}$	6.5	10.9	82.6	0.60	0.13
$Cu_{64}Zr_{36}$	2.1	13.1	84.7	0.16	0.15

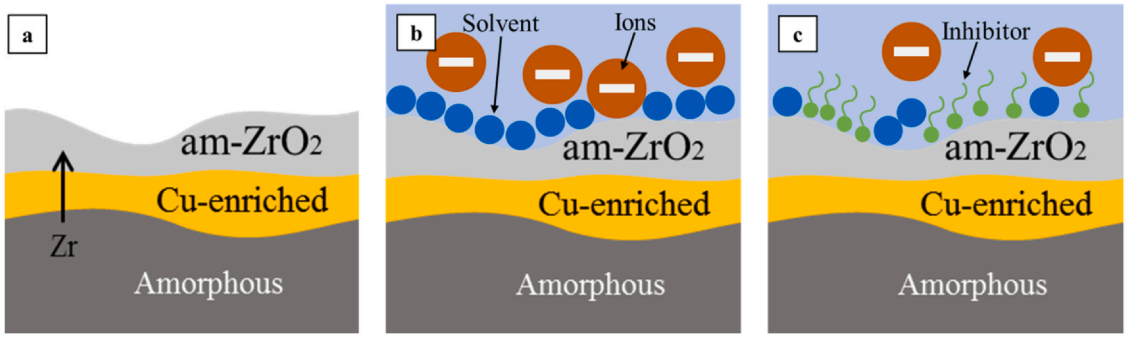

Fig. 5. Schematic of interface structure between electrode and electrolyte. (a) Native oxide layer of CuZr amorphous alloy. (b-c) Simple model for the interface between CuZr amorphous and electrolyte (b) without and (c) with inhibitor in solution.

Young's model [34–36], which assumes that the nonstoichiometry of the oxide film generates an exponential variation of the conductivity with respect to the normal distance to the electrode. In this model the measured impedance ($Z_{Y,oxide}$) is given by:

$$Z_{Y,oxide} = \frac{\lambda}{j\omega\varepsilon\varepsilon_0} ln\left(\frac{1 + j\omega\rho_0\varepsilon\varepsilon_0}{1 + j\omega\rho_0\varepsilon\varepsilon_0 exp(-\delta/\lambda)}\right) \quad (1)$$

where $j = \sqrt{-1}$, ω is the angular frequency, ε is the dielectric constant of the oxide film, ε_0 is permittivity of vacuum, δ is the film thickness, ρ_0 is resistivity at a position of spatial coordinate perpendicular to the electrode surface equal to 0, and λ is a material dependent parameter. According to Eq. (1), the Nyquist plot of a dielectric passive film shows a depressed semicircle, and for decreasing frequencies the impedance depends essentially on the resistivity of the film (Fig. 5b). After adsorption of inhibitors the impedance of the layer will increase, due to their dielectric nature (Fig. 5c). Thus, the impedance modulus at 0.01 Hz, labeled as $|Z|_{0.01\,Hz}$, will be used as a reference value to reflect the initial inhibition performance of the organic compounds. This initial performance allows us to select the most promising organic compounds and assess their performance on long-term tests. The results for the most promising inhibitors were additionally modeled using equivalent electrical circuits.

3.2.1. Electrochemical measurements in NaCl solution

Fig. 6 shows the Bode and Nyquist plots of CuZr alloys as well as of Cu and Zr pure metals. Zr metal exhibits better protective characteristics than Cu metal, as evidenced by (i) a broad range of linear increase of impedance modulus with frequency and larger impedance values over the whole frequency range (Fig. 6a); (ii) a broad range of frequency where phase angle is constant at values of about −80° indicating strong capacitive behavior (Fig. 6c); and (iii) much larger diameter of the Nyquist plot indicating much larger overall resistance (Fig. 6e) [36].

Crystalline alloys, considered in Fig. 6a, show reduced values of low frequency impedance as the Zr content decreases. $Cu_{40}Zr_{60}$ shows an impedance behavior close to that of pure Zr, but both $Cu_{50}Zr_{50}$ and $Cu_{64}Zr_{36}$ have impedances even lower than that of pure Cu. Analogously, the phase angle plots of $Cu_{50}Zr_{50}$ and $Cu_{64}Zr_{36}$ crystalline alloys reached a maximum at middle frequency range and then decreased to ca. −20° indicating the initiation of corrosion process (Fig. 6c). This behavior is attributed to the different crystalline phases present in these alloys (Fig. 2c), with different corrosion resistance, as well as to the existence of preferential corrosion sites at grain boundaries. These features are also shown in the Nyquist plot (Fig. 6e), which shows spurious behavior in some of the alloys. In contrast, the corrosion behavior of the amorphous alloys (Fig. 6b,d,f) is similar to that of pure Zr, showing strong capacitive behavior (Fig. 6b,d) and large semicircle (Fig. 6f) as expected for the aforementioned Young's model.

Interestingly, the low frequency impedance of amorphous $Cu_{50}Zr_{50}$ is somewhat larger than that of pure Zr (inset of Fig. 6b), while those of $Cu_{40}Zr_{60}$ and $Cu_{64}Zr_{36}$ are lower than that of pure Zr. According to the model presented in Fig. 5, larger Zr concentration should stimulate the development of the protective amorphous ZrO_2 dielectric layer. The fact that the equiatomic alloy shows the larger low frequency impedance after one hour seems to indicate that not only the Zr concentration is important for the creation of the ZrO_2 film, but also the atomic mobilities of Cu, Zr and O play an important role [37]. Given its smaller atomic size, Cu is known to have a large diffusivity in metallic glasses [38]. Thus, the development of the amorphous ZrO_2 layers in the Zr-rich amorphous alloys is probably delayed by the lower atomic mobility Fig. 7.

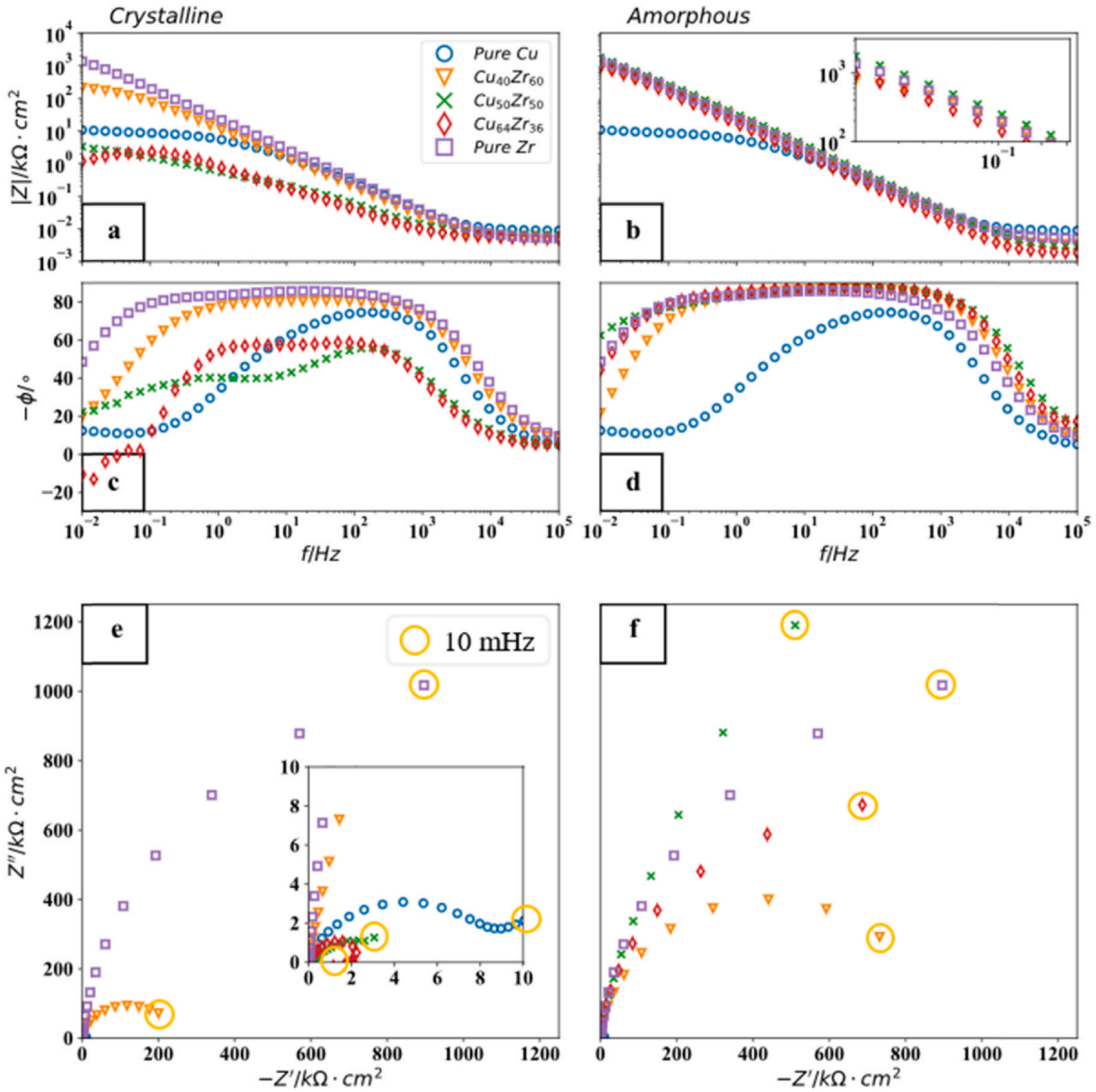

Fig. 6. Electrochemical impedance spectra in the form of (a,b) Bode impedance magnitude plot, (c,d) phase angle plot, and (e,f) Nyquist plot recorded for crystalline (left) and amorphous (right) alloys as well as Cu and Zr metals in aqueous 3 wt% NaCl solution after 1 h at the open circuit conditions.

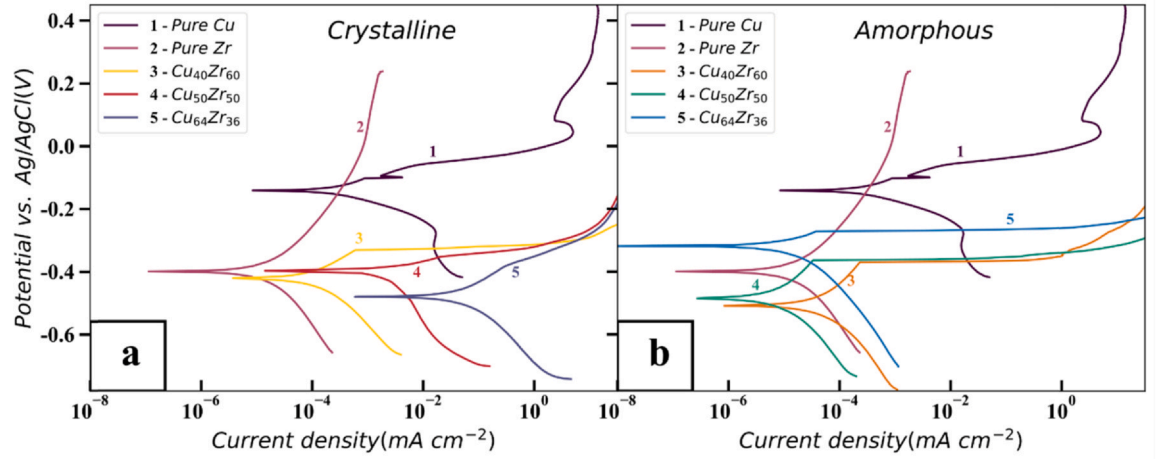

Fig. 7. Potentiodynamic curves for Cu, Zr, and crystalline and amorphous Cu_xZr_{100-x} alloys in 3 wt% NaCl. Quantitative electrochemical parameters are presented in Tables S1 and S2.

Fig. 7 shows the potentiodynamic polarization curves of Cu and Zr in NaCl. In chloride solution copper shows a well-known curve with cathodic reaction related to reduction of oxygen and anodic reaction related to dissolution of copper as cuprous Cu(I) species [19]. Current density increased starting from corrosion potential at −0.14 V up to an anodic peak at ~0 V when the formation of CuCl occurred [39,40]. At more positive potentials the current density shortly decreased but then it increased again due to formation of soluble cupric complexes [39,40]. In contrast, for Zr metal a rather broad passive range was established; following the E_{corr} at −0.40 V, passive range extended up to potentials above 0.2 V. Tables S1 and S2 in the Supplementary material provide more data on the quantitative electrochemical parameters derived from the polarization curves.

All three crystalline alloys exhibit worse corrosion resistance than Zr metal and the curves resemble more to that of Cu. Regarding the alloy composition, the corrosion parameters deteriorate with decreasing Zr content, as evidenced by the increasing corrosion current density (Tables S3–S8). The position of E_{corr} values is closer to that of Zr metal than that of Cu. However, compared to Zr metal, which shows a broad passive region, all crystalline and amorphous alloys show much narrower range between E_{corr} and abrupt increase in current density at more positive potentials. Amorphous alloys exhibit better performance than crystalline counterparts and smaller difference depending on Cu content that crystalline alloys (Fig. 7, Tables S3–S8).

3.2.2. XPS analysis of CuZr samples immersed in NaCl

High energy resolution XPS spectra recorded on the surface of amorphous and crystalline alloys after 24 h immersion in 3 wt% NaCl solution are presented in Figs. 3 and 4; the related chemical compositions are given in Tables 1 and 2. For amorphous alloys no significant change was observed (Fig. 3). ZrO_2 remained the predominant oxide. For $Cu_{40}Zr_{60}$ and $Cu_{50}Zr_{50}$ alloys the ZrO_2 peak shifted to a slightly higher energy, presumably related to further oxidation during immersion. For $Cu_{64}Zr_{36}$ alloy, opposite shift was observed, probably due to partial degradation of the oxide layer formed on this less corrosion resistant alloy.

For crystalline alloys, the immersion in NaCl caused more changes on the surface. For $Cu_{40}Zr_{60}$ and $Cu_{50}Zr_{50}$ alloys the concentration of Cu increases with immersion (Table 2) indicating enrichment of the layer with Cu. XPS spectra prove that during immersion not only cuprous Cu(I) oxide but also cupric Cu(II) species are formed because the Cu(II) satellite peak appears in the Cu 2p spectra (Fig. 4). The presence of cupric species in chloride containing solution is usually related to layer dissolution and formation of soluble copper chloride complexes [20]. These results corroborate electrochemical results stating that CuZr crystalline alloys exhibit lesser corrosion resistance than CuZr amorphous alloys regardless the alloy concentration.

3.3. Characterization of Cu and Zr metals and CuZr alloys in NaCl solution with added organic compounds

3.3.1. Short-term electrochemical results for Cu and Zr metals

Potentiodynamic polarization curves and quantitative electrochemical parameters derived from the polarization curves for Cu in the presence of potential inhibitors are presented in Fig. 8 and Table S1 in the Supplementary material, respectively. The effect of the organic compounds for the pure metals is diverse. In the case of Cu in NaCl solution, ImiH acted as an activator, while SH-ImiH-4Ph and SH-ImiMe acted as inhibitors causing a decrease in current density and shift in E_{corr} to more anodic values [20,29]. Two mercapto-based derivatives showed even better performance with the corrosion current densities j_{corr} decreasing in the following order: j_{corr}(SH-BimH) > j_{corr}(Me-S-BimH), whereas SH-BimH-5OMe and SH-BimH-$5NH_2$ acted as activators. Hydroxybenzimidazole derivatives also acted as corrosion activators. Efficient inhibitors on Cu acted as mixed type inhibitors with a strong inhibition on anodic reaction.

Different performance was observed for pure Zr when inhibitors are added to chloride solution (Fig. 8). Imidazole derivatives showed no inhibition activity. The SH-BimH-$5NH_2$ acted as the most efficient among mercaptobenzimidazoles, causing the largest shift of the E_{corr} to negative values and thus increasing the passive range; however, the j_{corr} was not significantly affected. In contrast to Cu, SH-BimH-5OMe acted as an activator, whilst SH-BimH and Me-S-BimH acted as very mild inhibitors. Hydroxybenzimidazole derivatives also acted as activators. Efficient inhibitors on Zr behave as cathodic type inhibitors. Quantitative electrochemical parameters derived from the polarization curves for Zr presented in Fig. 8 are given in Table S2 in the Supplementary material.

EIS spectra recorded for Cu and Zr metals after 1 h immersion in NaCl containing organic compounds are presented in Figs. S3–S5 in the Supplementary material. For Cu, SH-ImiH-4Ph and SH-ImiMe acted inhibitive, as well as all mercaptoimidazole derivatives except SH-BimH-$5NH_2$, whereas for Zr metal, the EIS response in the presence of organic compounds is less affected.

Comparison of the inhibition efficiency of the tested molecules is not straightforward. On the one side, the presence of a uniform dielectric film on the alloy surface makes it impossible to use common linear sweep methods to evaluate the inhibition effect. On the other side, the Nyquist plots shown in Figs. S3–S5 show clearly that different inhibitors could be fitted using different equivalent circuits. No general model can be fitted to the recorded data, and intercomparison is not possible with different electrochemical descriptions. Hence, we pursue here a feasible and simple approach that utilizes as a comparison parameter the impedance modulus at 10 mHz, denoted as $|Z|_{0.01\,Hz}$. Fitting to electrochemical equivalent circuits is restricted only to those inhibitor/alloy combinations that show a positive interaction in this first screening, and is presented below. The validity of $|Z|_{0.01\,Hz}$ as a measure of the inhibition efficiency relies on two facts: the low frequency impedance correlates to the combined effect of diffusion and charge transfer and it shows a huge drop in the case of localized pitting. Besides, such parameter is adequate for fast screening.

The measured values of $|Z|_{0.01\,Hz}$ in the solutions containing the studied organic compounds are presented in Fig. 9. It is evident that organic compounds added to NaCl affect significantly the behavior of Cu but only insignificantly that of Zr. The effect will be discussed further in Section 4.

3.3.2. Short-term electrochemical results for CuZr alloys

3.3.2.1. $Cu_{40}Zr_{60}$. Polarization curves and quantitative electrochemical parameters derived from the polarization curves for $Cu_{40}Zr_{60}$ alloys are presented in Fig. 10 and Tables S3–S4 in the Supplementary material, respectively. The inhibition performance of all inhibitors is poor for the $Cu_{40}Zr_{60}$ crystalline alloy, as dissolution, indicated by the increase in current density, initiates in the anodic branch at a similar potential, regardless the inhibitor. A more diverse behavior is observed for the amorphous samples, where several of them act as cathodic inhibitors as in the case of pure Zr.

EIS spectra recorded for $Cu_{40}Zr_{60}$ crystalline and amorphous alloys after 1 h immersion in NaCl containing organic compounds are presented in Figs. S6–S8 in the Supplementary material. The comparison of $|Z|_{0.01\,Hz}$ again shows much larger impact of inhibitors on crystalline alloys than on amorphous alloys which show better corrosion performance (Fig. 9).

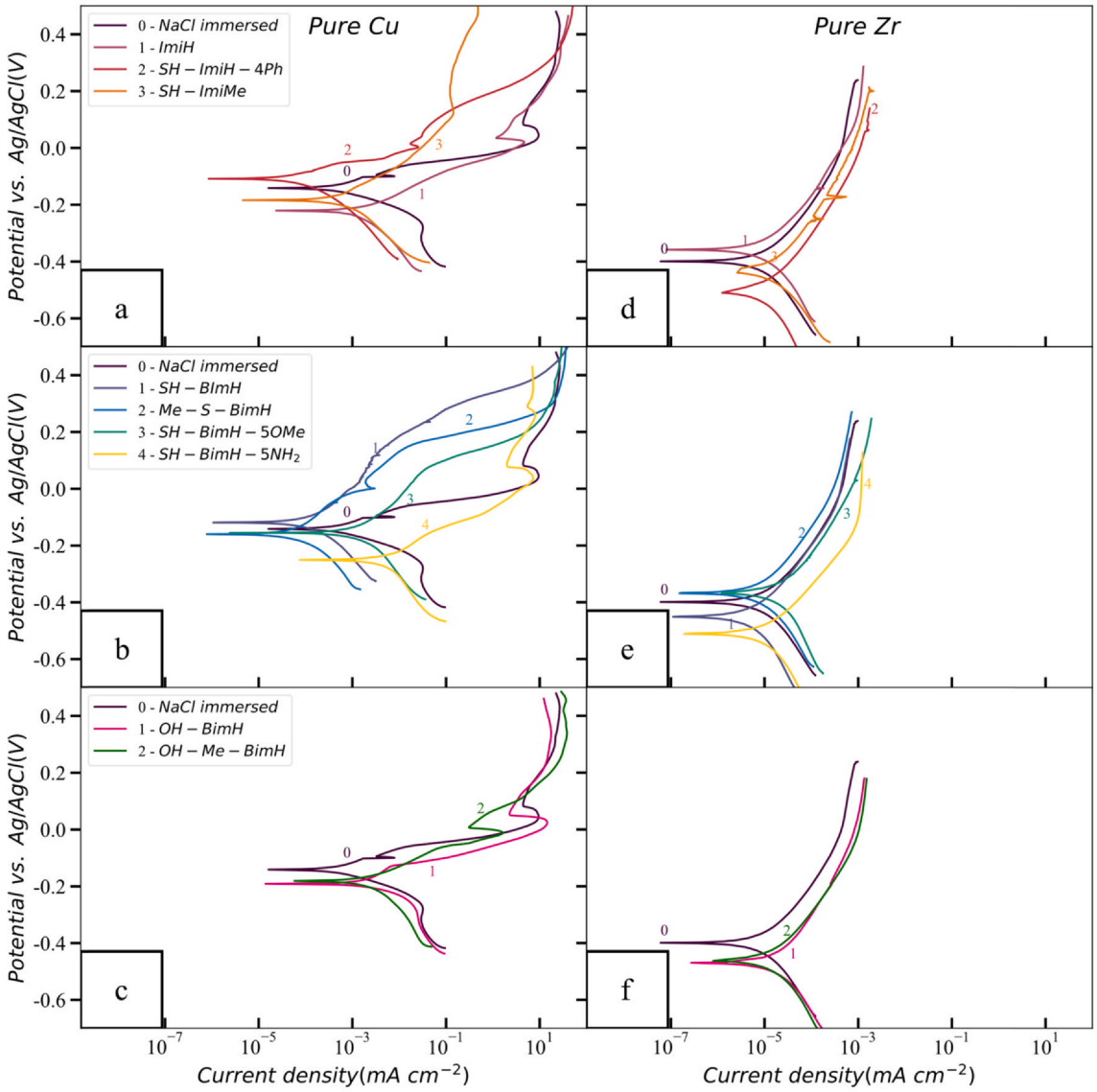

Fig. 8. Potentiodynamic polarization curves of Cu (left) and Zr (right) in 3 wt% NaCl aqueous solution with and without 1 mM of different organic compounds: (top) imidazole derivatives, (middle) mercaptobenzimidazole derivatives, and (bottom) hydroxybenzimidazole derivatives. Quantitative electrochemical parameters are presented in Tables S1 and S2.

3.3.2.2. $Cu_{50}Zr_{50}$. None among compounds tested shows any inhibition properties on crystalline $Cu_{50}Zr_{50}$ alloy. The potentiodynamic polarization curves are quite similar for solutions with and without organic inhibitors as shown in Fig. 11. With inhibitors added, in the cathodic range the current density is slightly decreased but in the anodic range a fast dissolution of the alloy takes place, similar as in the absence of inhibitor. Amorphous $Cu_{50}Zr_{50}$ shows slightly better performance than crystalline alloy. A passive range is induced on the sample, both in the non-inhibited and inhibited solutions. When adding imidazole-based derivatives, SH-ImiH-4Ph showed the best performance, shifting the E_{corr} more negative and decreasing the cathodic current density. Even more pronounced inhibitive behavior was observed for mercaptobenzimidazole derivatives, with SH-BimH-5OMe being the most efficient (Fig. 11e) as it increased slightly the pitting potential. Both hydroxy-derivatives acted as corrosion activators (Fig. 11f). Quantitative electrochemical parameters derived from the polarization curves for $Cu_{40}Zr_{60}$ alloys are presented in Tables S5–S6 in the Supplementary material.

EIS spectra recorded for $Cu_{50}Zr_{50}$ crystalline and amorphous alloys after 1 h immersion in NaCl containing organic compounds are presented in Figs. S9–S11 in the Supplementary material. The comparison of short term EIS behavior is given in Fig. 9.

3.3.2.3. $Cu_{64}Zr_{36}$. Almost no inhibition effect was achieved with any of the compounds for crystalline or amorphous samples of $Cu_{64}Zr_{36}$ in 3 wt% NaCl aqueous solution in the presence of the organic compounds studied, as shown in Fig. S12 in the Supplementary material. Quantitative electrochemical parameters derived from the polarization curves for $Cu_{40}Zr_{60}$ crystalline and amorphous alloys are presented in Tables S7 and S8 in the Supplementary material. Due to fast dissolution of materials, the Tafel parameters could not be determined for crystalline $Cu_{64}Zr_{36}$.

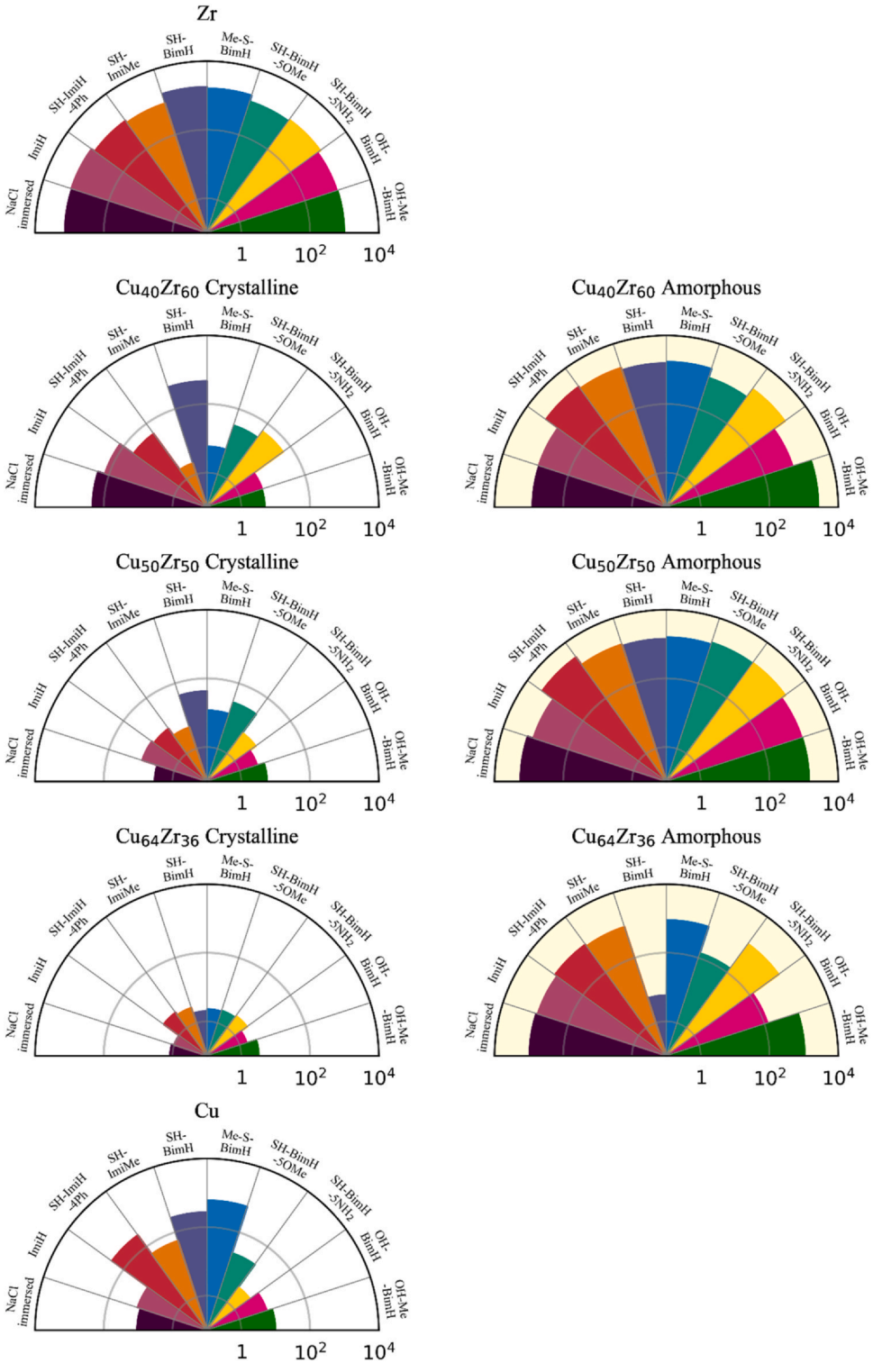

Fig. 9. Polar graphs of impedance modulus (given in kΩ cm^2) at 0.01 Hz, measured after 1 h immersion, for Zr (top) and Cu (bottom) metals and crystalline (left) and amorphous (right) Cu_xZr_{100-x} alloys in 3 wt% NaCl aqueous solution (blank) and in the presence of different organic compounds added at 1 mM concentration. Note the logarithmic scale.

EIS spectra recorded for $Cu_{64}Zr_{36}$ crystalline and amorphous alloys after 1 h immersion in NaCl containing organic compounds are presented in Figs. S13–S15 in the Supplementary material. The comparison of short term EIS behavior is given in Fig. 9.

3.3.2.4. Modeling of EIS data. Based on potentiodynamic and EIS results on amorphous alloys, three inhibitors were selected for further study using modeling of EIS data. In contrast, the inhibitive effect of organic compounds on crystalline alloys is too weak and, therefore, it will not be studied further by EIS modeling.

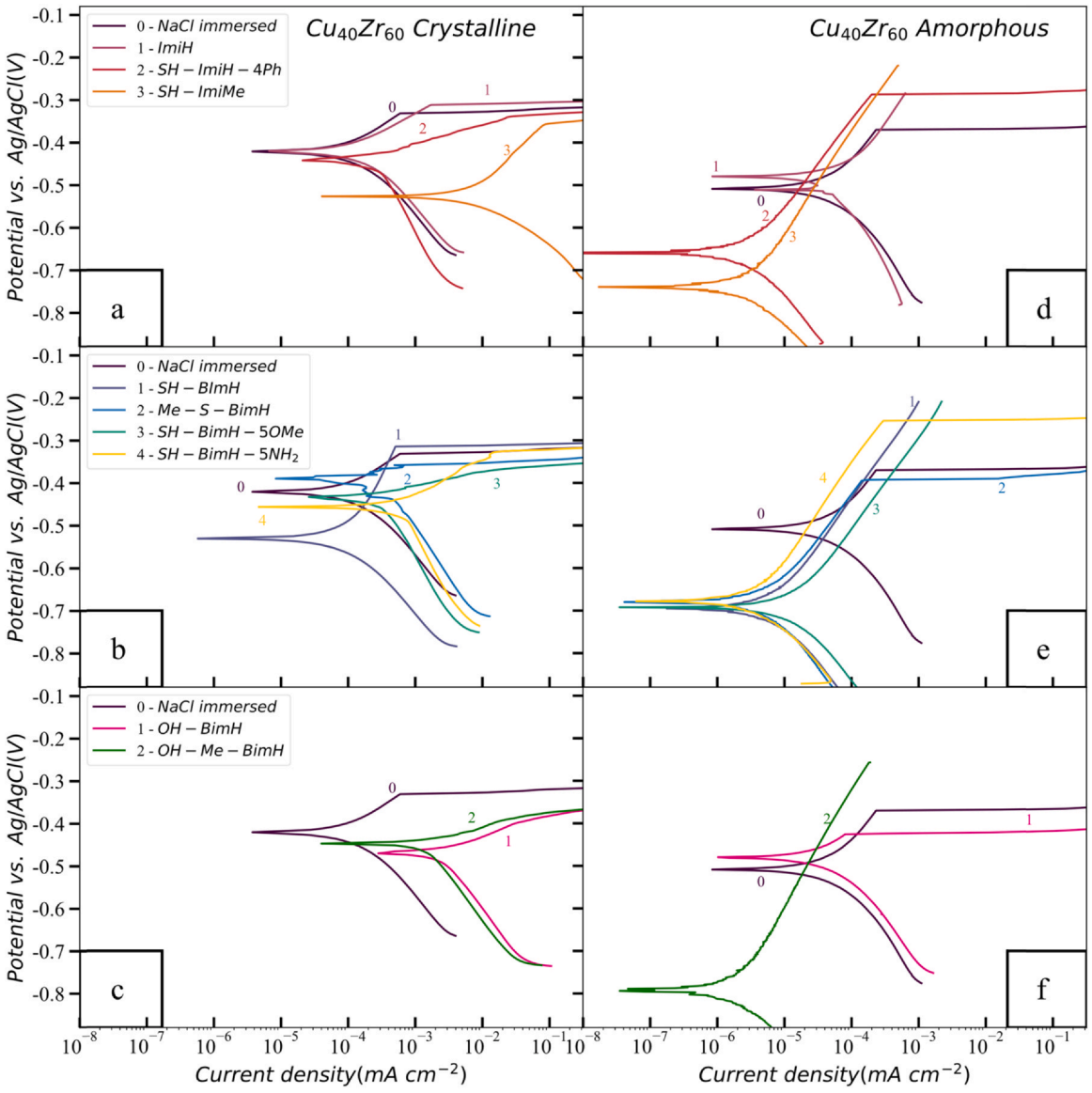

Fig. 10. Potentiodynamic polarization curves of crystalline (left) and amorphous (right) $Cu_{40}Zr_{60}$ in 3 wt% NaCl aqueous solution with and without 1 mM of different organic compounds: (top) imidazole derivatives, (middle) mercaptobenzimidazole derivatives, and (bottom) hydroxybenzimidazole derivatives. Quantitative electrochemical parameters are presented in Tables S3 and S4.

As shown by the XPS data (Figs. 3 and 4), the uniform oxidation of amorphous CuZr alloy and pure Zr results in a dielectric ZrO_2 film covering the surface [31]. The charge transfer resistance is high and the corrosion current is low, as shown by Tafel parameters tabulated in Tables S2, S4, S6 and S8. Thus, two simple equivalent electric circuits (EEC) were selected to model the amorphous alloy/electrolyte interface with and without inhibitors (Fig. 12). As the Warburg resistance is negligible in these systems, in the absence of inhibitor only the resistance of the solution (R_s), the charge transfer resistance (R_{ct}) and the capacitance of oxide layer and double layer (Q_o) are taken into consideration [41,42]. In the presence of inhibitor, the adsorbed organic molecules modify the EIS response of the ZrO_2 layer, hence the capacitance (Q_f) and the resistance of the inhibitor film (R_f) are added to the EEC. Fig. 13 shows the modeled and original Nyquist plots and Bode plots of the amorphous alloy $Cu_{40}Zr_{60}$ (fitted EIS data are in Table S9). Fitted EIS data for the other two amorphous alloys are given in Figs. S16 and S17 and Tables S10 and S11 in the Supplementary material. The sum of R_{ct} and R_f is equal to the polarization resistance (R_p) [43], where the R_{ct} parameter is the charge-transfer resistance describing the faradaic reaction at the metal/electrolyte solution interface occurring as a result of structure defects in the layer upon immersion in NaCl solution and R_f is the resistance of the inhibitor layer. The value of R_p reflects the corrosion rate of the metal according to the theory of the kinetics for corrosion processes at the metal/electrolyte solution interface [44].

Herein, results are presented graphically as R_p for all three amorphous alloys (Fig. 14). The higher values of R_p are obtained for $Cu_{40}Zr_{60}$ and $Cu_{50}Zr_{50}$ in the presence of two selected inhibitors compared to the value in NaCl solution confirming the protective character of the adsorbed organic layer. For the $Cu_{64}Zr_{36}$, the R_p values are smaller than for the other two alloys reflecting poor corrosion performance of this alloy.

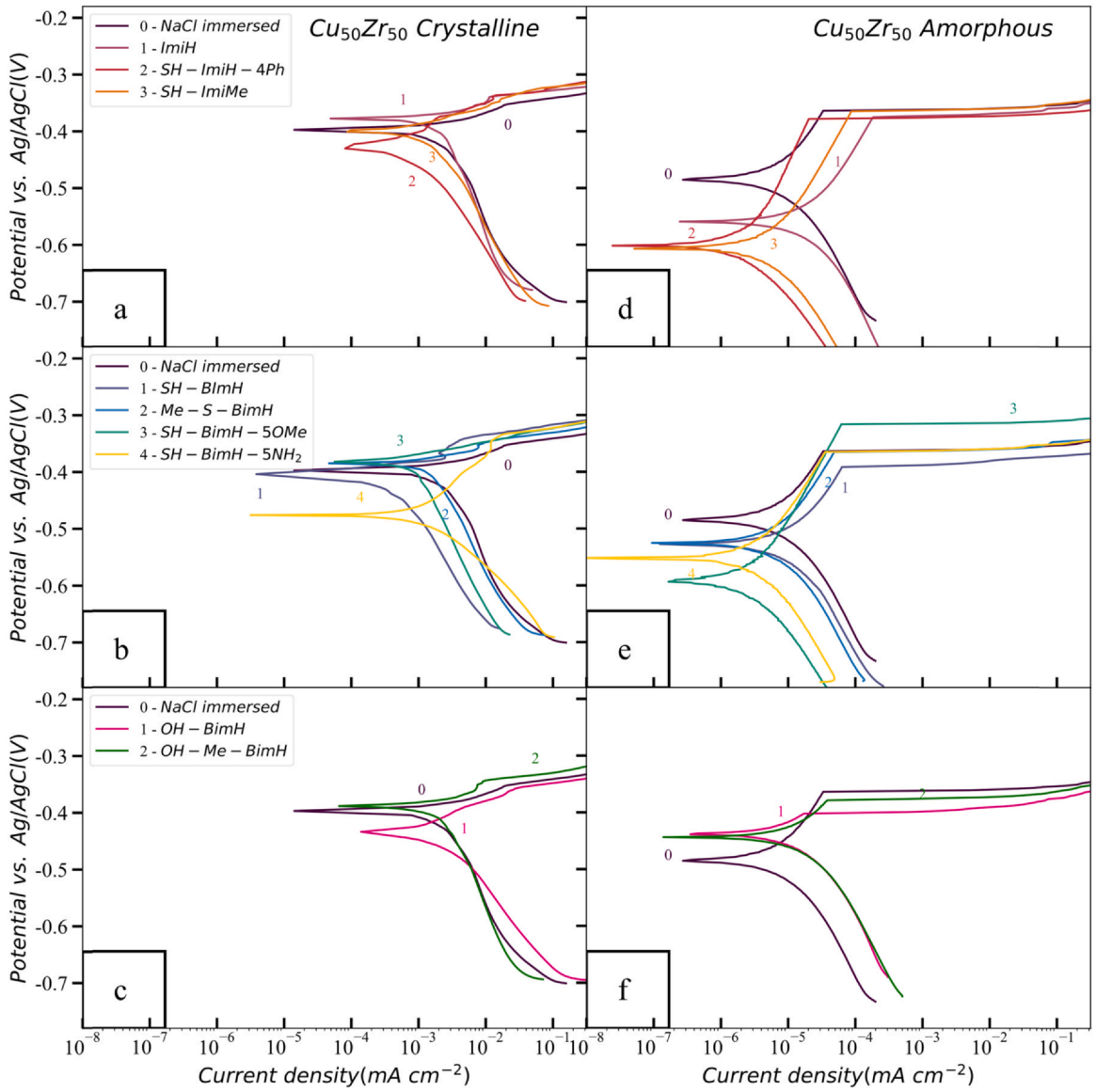

Fig. 11. Potentiodynamic polarization curves of crystalline (left) and amorphous (right) $Cu_{50}Zr_{50}$ in 3 wt% NaCl aqueous solution with and without 1 mM of different organic compounds: (top) imidazole derivatives, (middle) mercaptobenzimidazole derivatives, and (bottom) hydroxybenzimidazole derivatives. Quantitative electrochemical parameters are presented in Tables S5 and S6.

3.3.3. *Long-term electrochemical and microscopy results*

Time-resolved performance of the studied inhibitors was determined by measuring the EIS spectra of the crystalline and amorphous alloys over an immersion time of 120 h in the presence of the most promising inhibitors, chosen from the results of potentiodynamic polarization measurements (Figs. 10, 11 and S12). Fig. 15 displays in a compact way the long-term EIS behavior of the alloys in blank NaCl and with added inhibitors selected for each alloy.

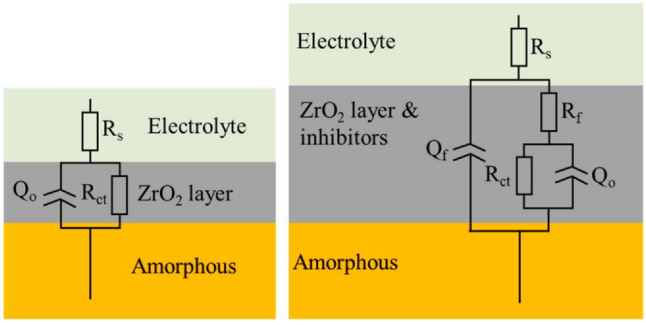

Fig. 12. Schematic equivalent electric circuits for amorphous alloys in NaCl (left) and NaCl with added inhibitors (right).

The $|Z|_{0.01\ Hz}$ of the amorphous $Cu_{40}Zr_{60}$ alloy in chloride solution was about two orders of magnitude higher than that of the crystalline alloy. In the presence of SH-ImiMe, SH-ImiH-4Ph and SH-BimH-$5NH_2$ the low frequency impedance values remained two orders of magnitude higher than those of the crystalline samples, and even showed a small but steady increase with time which may correspond to the formation of a passive film. The EIS findings are confirmed by direct observation of the samples after 5 days immersion tests. Fig. 16 shows the SEM images of the $Cu_{40}Zr_{60}$ amorphous samples in the presence of several inhibitors. The most protected surface was the one corresponding to the immersion in the presence of SH-ImiMe (Fig. 16e). Other samples showed some corrosion damage.

The initial $|Z|_{0.01\ Hz}$ values in NaCl for crystalline $Cu_{50}Zr_{50}$ were smaller than those for $Cu_{40}Zr_{60}$, whereas for amorphous alloys were

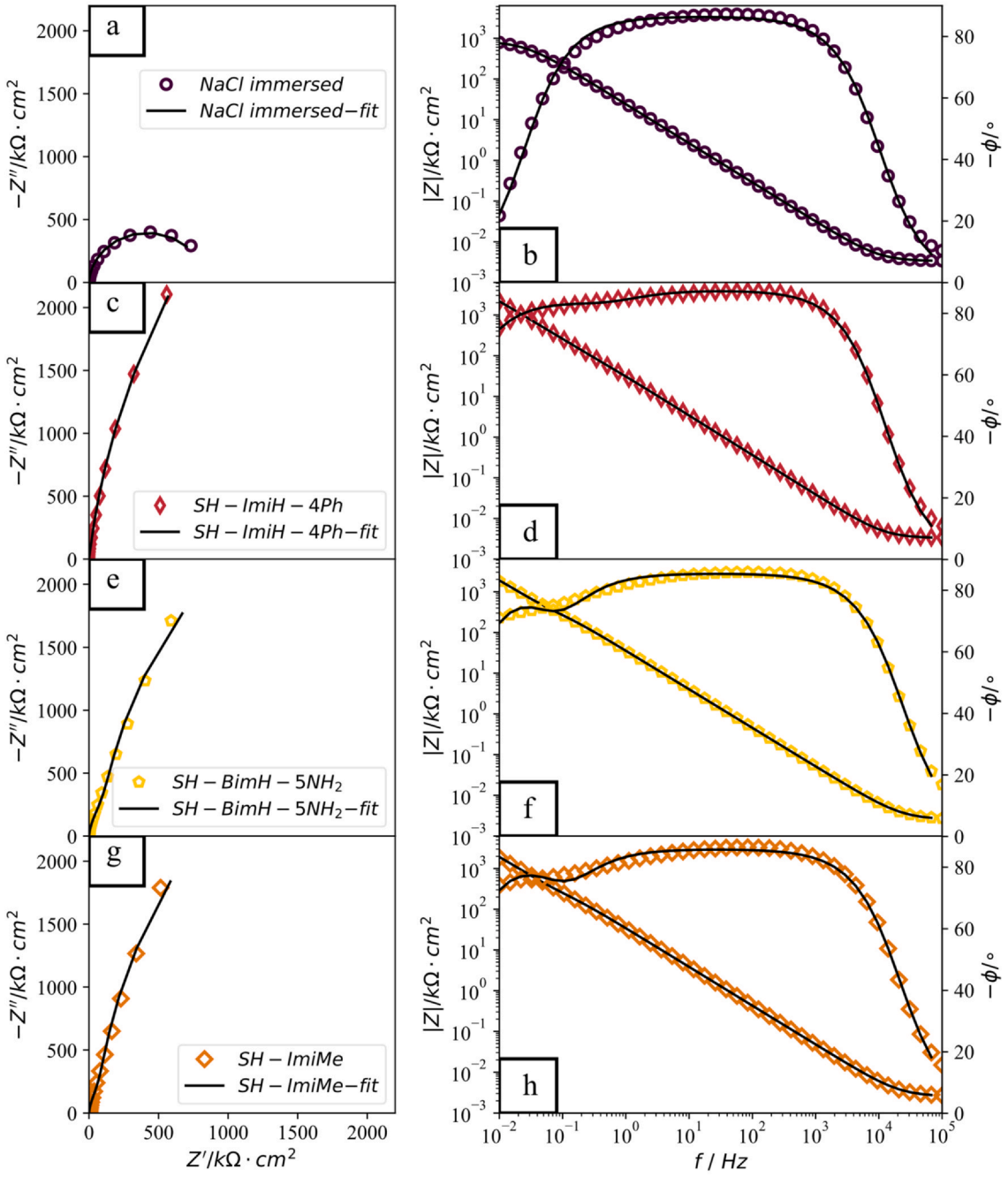

Fig. 13. Measured (symbols) and modeled (solid line) Nyquist plots (right) and Bode plots (left) of $Cu_{40}Zr_{60}$ amorphous alloy recorded after 1 h immersion in (a,b) 3 wt% NaCl, and with added (c,d) SH-ImiH-4Ph, (e,f) SH-BimiH-5NH_2, and (g,h) SH-ImiMe.

similar (Fig. 15). However, amorphous $Cu_{50}Zr_{50}$ alloy deteriorated noticeably with time. The best inhibition ability was shown by SH-BimH-5NH_2, which kept a high and quite stable impedance in all measurements. The performance of SH-BimH-5OMe and SH-ImiH-4Ph decreased as a consequence of an incipient pitting process. SEM images confirm that among $Cu_{50}Zr_{50}$ crystalline samples only the sample immersed in NaCl with added SH-BimH-5NH_2 (Fig. 17e) was able to remain without apparent pitting after immersion over 5 days. Some inhibitors were not able to protect the alloys (SH-BimH-5OMe, SH-ImiH-4Ph, OH-Me-BimH) and after 60 h a sudden decrease is observed for blank (NaCl) and OH-Me-BimH samples (Fig. 15). Following the breakdown, either the sample was partially dissolved or the surface was covered by corrosion products, and EIS measurements were no longer trustable.

The long-term EIS measurements confirmed a low corrosion resistance of $Cu_{64}Zr_{36}$ alloys, which quickly deteriorate with time (Fig. 15), as evidences also by SEM images (Fig. S18).

4. Discussion

The summarized comparison of impedance modulus at 0.01 Hz ($|Z|_{0.01\ Hz}$) of Cu and Zr metals as well as of all the tested crystalline

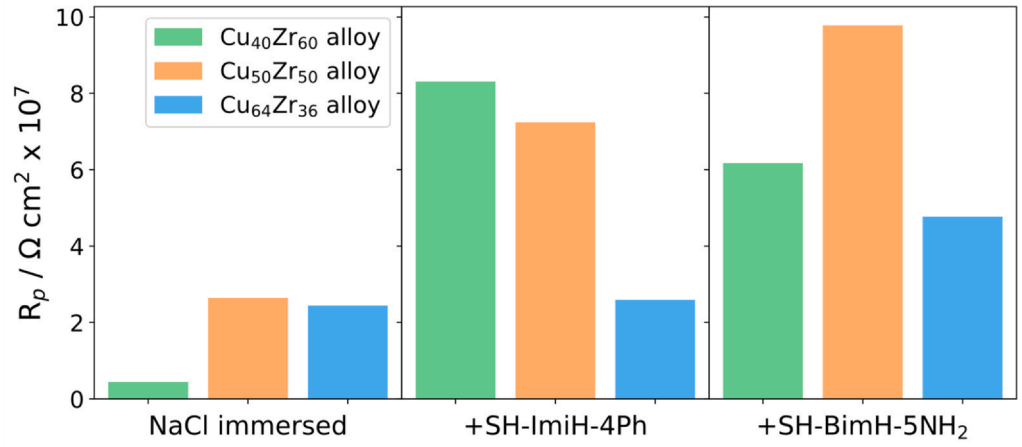

Fig. 14. Polarization resistance (R_p) of $Cu_{40}Zr_{60}$, $Cu_{50}Zr_{50}$ and $Cu_{64}Zr_{36}$ amorphous alloys with and without added 1 mM inhibitor compounds (either SH-ImiH-4Ph or SH-BimH-5NH$_2$) in 3 wt% NaCl solution.

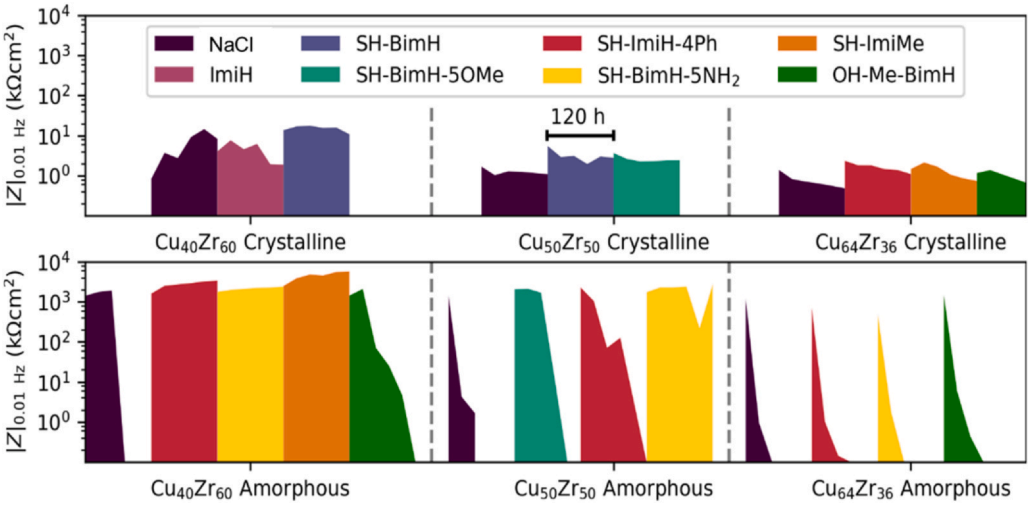

Fig. 15. Long-term tests of the impedance modulus at 0.01 Hz in the presence of selected inhibitors. Each bar corresponds to the 120 h period of testing of the alloy in the presence of the inhibitor in the 3 wt% NaCl aqueous solution.

and amorphous alloys after immersion for 1 h in 3 wt% NaCl aqueous solution is shown in Fig. 9. Some of the inhibitors appear beneficial for Cu, particularly the mercapto compounds Me-S-BimH, SH-BimH, SH-ImiH-4Ph and SH-ImiMe, as they increase the low frequency impedance by a factor of 10 or more compared to that in blank NaCl solution. Contrarily, the low frequency impedance of Zr in the presence of all tested inhibitors is very similar to that of blank Zr. It is therefore clear that the inhibition efficiency of the selected inhibitors on Cu is much higher than on Zr.

As for the crystalline alloys, the inhibition performance, deduced either from reduced current density or impedance modulus, of all the inhibitors is rather limited. Even the best case is not able to reach the low frequency impedance of non-inhibited Zr. The corrosion resistance of Zr is rapidly degraded by the addition of Cu. The corrosion resistance of all crystalline alloys in the presence of any organic compound is lower than that of bare Zr. As an example, the inhibition performance of Me-S-BimH, which is the best inhibitor for Cu and almost neutral for Zr, is clearly lower for all the crystalline alloys. This is attributed to the presence of different crystalline phases, and especially the corresponding grain boundaries which may become preferential sites for accelerated corrosion.

Amorphous alloys, on the contrary, show a different behavior (Fig. 9). All three amorphous alloys show an intrinsic corrosion resistance similar to that of bare Zr. The performance of all tested compounds for amorphous $Cu_{40}Zr_{60}$ and $Cu_{50}Zr_{50}$ is similar. In both cases, SH-ImiH-4Ph increases substantially the low frequency impedance. SH-BimH, Me-S-BimH, SH-BimH-5NH$_2$, SH-ImiMe and OH-Me-BimH are also protective for $Cu_{40}Zr_{60}$. However, all organic compounds are neutral or even accelerate corrosion for $Cu_{64}Zr_{36}$. It is worth to mention that the phase diagram (Fig. S2) shows that the stable phase for this composition is a solid solution of Cu_8Zr_3 and $Cu_{10}Zr_7$, present in the crystalline alloy (Fig. 2e) [30]. Because the chemical composition of the CuZr amorphous alloy varies continuously, the atomic environments are changing and the intrinsic topology changes with them. According to the solute centered cluster model [45], slight changes in the atomic composition affect significantly the packing efficiency [46] and inhibitor–surface interaction responds to these changes, which is presumably critical for

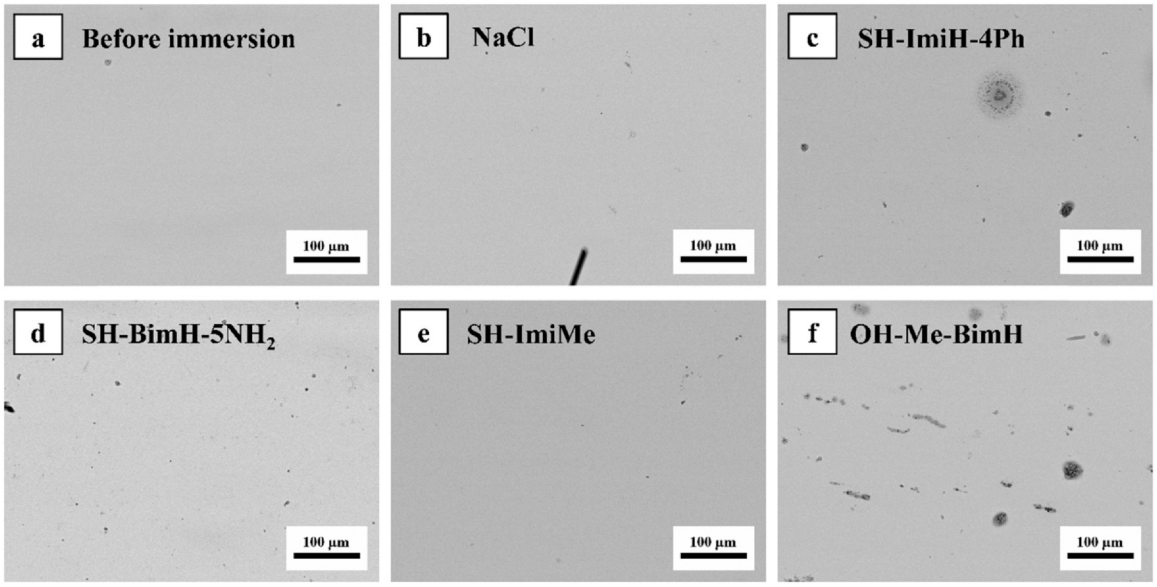

Fig. 16. SEM images of $Cu_{40}Zr_{60}$ amorphous alloy (a) prior to immersion and after 120 h immersion in (b) 3 wt% NaCl with added (c) SH-ImiH-4Ph, (d) SH-BimH-5NH_2, (e) SH-ImiMe, and (f) OH-Me-BimH.

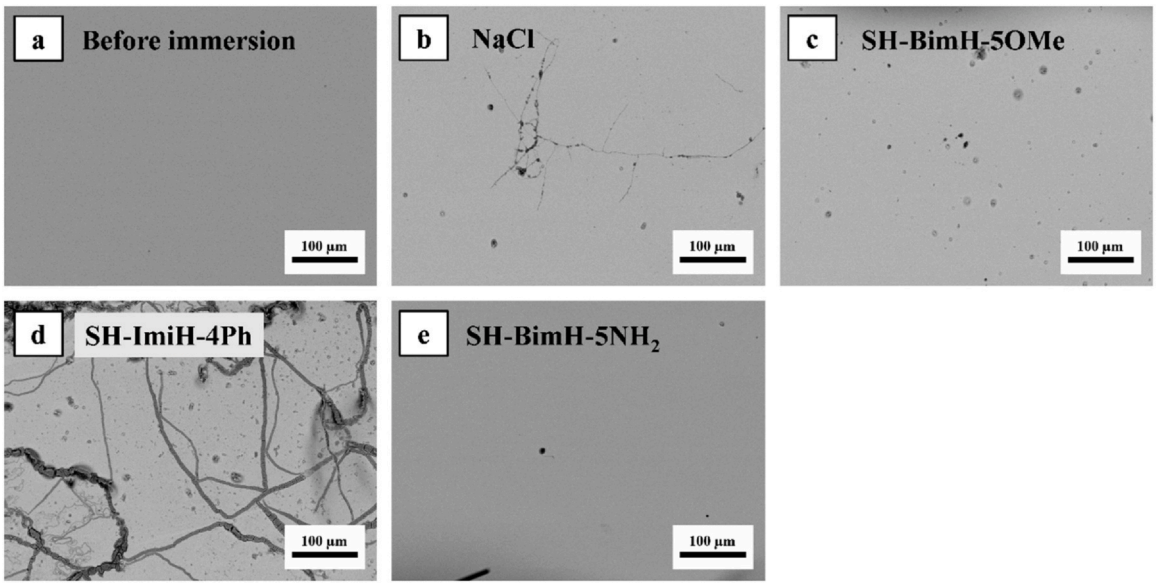

Fig. 17. SEM images of $Cu_{50}Zr_{50}$ amorphous alloy (a) prior to immersion and after 120 h immersion in (b) 3 wt% NaCl, and with added (c) SH-BimH-5OMe, (d) SH-ImiH-4Ph, and (e) SH-BimH-5NH_2.

the corrosion resistance. Furthermore, by changing the Cu/Zr atomic ratio, the solute/solvent role of the atoms becomes inverted and both the glass structure and the atomic diffusivities must inevitably be different. These facts in turn affect the formation of the ZrO_2 rich layer on top of the amorphous surface (Figs. 3 and 5). Zr-rich amorphous alloys may show lower diffusivities which initially may hinder the formation of the amorphous ZrO_2 film, but in the long term they eventually develop passivation layers that in combination with the proper inhibitors prevent localized corrosion. As the concentration of Zr is decreased, the ZrO_2 layer may be defective in Zr thus resulting in a mixed (CuZr)-oxide layer, which probably allows the removal of metallic ions. Thus, a Zr content equal or above 50% is needed for an adequate inhibition performance.

The comparison of the initial performance, measured after 1 h immersion, of the tested inhibitors for the crystalline and amorphous phases is summarized in Fig. 18. The inhibitor performances for bare Cu and Zr metals are shown on the diagonal, because bare metals lack the amorphous phase. It is clearly evident that (1) all the tested amorphous alloys show a much better corrosion resistance than their crystalline counterparts in the presence of inhibitors and that (2) amorphous $Cu_{40}Zr_{60}$ and $Cu_{50}Zr_{50}$ perform better than amorphous $Cu_{64}Zr_{36}$, in line with the aforementioned argument of the importance of the high content of Zr in alloys for corrosion resistance. In view of the saturation of the low frequency impedance for all the considered inhibitors it is therefore reasonable to conclude that the main factor controlling the corrosion resistance of the alloys is the Zr-rich (or at least equiatomic) amorphous structure, the effect of the inhibitor being secondary.

It is also worth to mention that the initial performance of the inhibitors is not sufficient to predict the long-term behavior of the

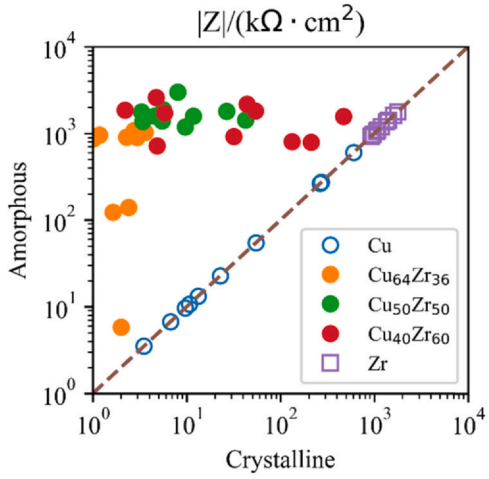

Fig. 18. Impedance modulus at 0.01 Hz, measured after 1 h immersion, of the alloys in the presence of the organic compounds, tested as corrosion inhibitors for the studied alloys (•). For comparison, also the values for bare Zr (□) and bare Cu (○) are plotted on the dashed diagonal line.

corrosion rate for the alloys. Fig. 15 shows that the long-term corrosion resistance degrades in all amorphous alloys except in $Cu_{40}Zr_{60}$ in the presence of SH-ImiH-4Ph, SH-BimH-5NH_2 and Sm-ImiMe, and in $Cu_{50}Zr_{50}$ in the presence of SH-BimH-5NH_2. SH-BimH-5NH_2 is, thus, the most effective inhibitor, provided the Zr concentration is high enough (≥ 50%). Of all the tested compounds, this was the single one containing the amino group. It is noteworthy that SH-BimH-5NH_2 does not perform well for bare Cu, although it was computed that interaction between the amino group and Cu is stronger than with Au and Ag [47]. Besides, there is evidence of formation of $ZrNH_3$ on annealing [48], which suggests some affinity of Zr for the amino group. This suggests that the good performance on Zr-rich alloys is consequence of the interaction of the amino group with Zr atoms. The long-term behavior, on the contrary, correlates much better with the results of modeled electrochemical data (Figs. 13 and 14).

5. Conclusions

Three Cu_xZr_{100-x} amorphous and crystalline alloys (x = 40, 50, 64 at%) were prepared and characterized in terms of microstructure, composition and electrochemical properties. Pure Cu and Zr metals were taken as reference materials. CuZr amorphous alloys are covered by a thin and homogeneous ZrO_2 layer, which is spontaneously formed on the surface. In contrast, crystalline alloys show higher Cu content than CuZr amorphous alloys. The main crystalline phase in $Cu_{40}Zr_{60}$ is identified to be $CuZr_2$, although it may also contain traces of $Cu_{10}Zr_7$. $Cu_{50}Zr_{50}$ is composed of $CuZr_2$ and $Cu_{10}Zr_7$, while $Cu_{10}Zr_7$ and Cu_8Zr_3 are identified in $Cu_{64}Zr_{36}$. The corrosion resistance of crystalline alloys in NaCl solution is substantially lower than that of bare Zr and even Cu metals. The corrosion resistance of amorphous alloys in NaCl solution is higher than that of crystalline alloys and more similar to Zr metal.

The inhibition performance of imidazole, mercaptobenzimidazole and hydroxybenzimidazole derivatives on CuZr crystalline and amorphous alloys was studied. We utilized impedance modulus at 0.01 Hz, measured after 1 h immersion, as a measure of the initial inhibitor performance. On the basis of this initial evaluation we selected the promising compounds for long-term tests. Amorphous alloys showed always a higher corrosion resistance than their crystalline counterparts. This fact is attributed to the coexistence of several intermetallic phases with different corrosion resistance and/or the reduced corrosion resistance of dislocations and grain boundaries in the studied alloys. The addition of corrosion inhibitors did not improve the corrosion resistance of the crystalline CuZr alloys, even those which showed a protective effect in bare Cu.

Amorphous alloys showed a good initial corrosion resistance even without inhibitors, similar to that of bare Zr. In alloys with high Zr content (equal or above 50 at%), the corrosion resistance is increased by the two tested mercaptoimidazole based inhibitors and all tested mercaptobenzimidazole based inhibitors. These data show that the homogeneous surface structure of amorphous alloys is much less prone to corrosion, and the tested corrosion inhibitors even improve it to some extent. However, the increase of the low frequency impedance modulus due to the presence of inhibitors tends to saturate regardless the organic compound in solution, showing that the determinant factor in the corrosion resistance is the smooth surface topology of amorphous alloys and the stability of the oxide layer.

The long-term corrosion resistance degrades except in $Cu_{40}Zr_{60}$ in the presence of SH-ImiH-4Ph, SH-BimH-5NH_2 and SM-ImiMe, and in $Cu_{50}Zr_{50}$ in the presence of SH-BimH-5NH_2. SH-ImiMe induces the highest polarization resistance of $Cu_{40}Zr_{60}$, but overall 5-amino-2-mercaptobenzimidazole is the most promising corrosion inhibitor in CuZr amorphous alloys. It is advised to deepen the study of the surface interaction of the amino group with these materials.

This work shows that long-term low impedance measurements are an adequate screening parameter in the determination of the corrosion inhibition efficiency.

CRediT authorship contribution statement

Chenyang Xie: Investigation, Data curation, Visualization, Writing. **Ingrid Milošev:** Methodology, Validation, Writing. **Frank U. Renner:** Funding acquisition, Validation, Writing. **Anton Kokalj:** Methodology, Validation, Writing. **Pere Bruna:** Investigation. **Daniel Crespo:** Funding acquisition, Methodology, Resources, Supervision, Validation, Visualization, Writing.

Declaration of Competing Interest

The authors declare that they have no known competing financial interests or personal relationships that could have appeared to influence the work reported in this paper.

Acknowledgements

This work is a part of M-Era.Net project entitled “CoinDesc: Corrosion inhibition and dealloying descriptors”. The financial support of the project by MICINN (Ministry of Science, Innovation and Universities of Spain, projects PCIN-2016-027 and FIS2017-82625-P), Generalitat de Catalunya (2017SGR00042), FWO G0H5516N (Research Foundation Flanders), and MESS (Ministry of Education, Science and Sport of Republic of Slovenia, Grant No. C3330–17-500074) is acknowledged. C. Xie was supported by the CSC (Chinese Scholarship Council, China) grant No. 201606460065.

Appendix A. Supporting information

Supplementary data associated with this article can be found in the online version at doi:10.1016/j.jallcom.2021.160464.

References

[1] P. Yu, H.Y. Bai, M.B. Tang, W.L. Wang, Excellent glass-forming ability in simple Cu50Zr 50-based alloys, J. Non Cryst. Solids 351 (2005) 1328–1332, https://doi.org/10.1016/j.jnoncrysol.2005.03.012

[2] O.J. Kwon, Y.C. Kim, K.B. Kim, Y.K. Lee, E. Fleury, Formation of amorphous phase in the binary Cu-Zr alloy system, Met. Mater. Int. 12 (2006) 207–212, https://doi.org/10.1007/BF03027532

[3] P. Yu, H.Y. Bai, W.H. Wang, Superior glass-forming ability of CuZr alloys from minor additions, J. Mater. Res. 21 (2006) 1674–1679, https://doi.org/10.1557/jmr.2006.0212

[4] W.H. Wang, The elastic properties, elastic models and elastic perspectives of metallic glasses, Prog. Mater. Sci. 57 (2012) 487–656, https://doi.org/10.1016/j.pmatsci.2011.07.001

[5] R. Ray, B.C. Giessen, N.J. Grant, Formation of Cu–Zr metallic glasses, Scr. Met. 2 (1968) 359.

[6] Y.C. Kim, J.C. Lee, P.R. Cha, J.P. Ahn, E. Fleury, Enhanced glass forming ability and mechanical properties of new Cu-based bulk metallic glasses, Mater. Sci. Eng. A. 437 (2006) 248–253, https://doi.org/10.1016/j.msea.2006.07.141

[7] Q. Zhang, W. Zhang, A. Inoue, New Cu-Zr-based bulk metallic glasses with large diameters of up to 1.5 cm, Scr. Mater. 55 (2006) 711–713, https://doi.org/10.1016/j.scriptamat.2006.06.024

[8] M. Naka, K. Hashimoto, T. Masumoto, Corrosion behavior of amorphous and crystalline Cu50Ti50 and Cu50Zr50 alloys, J. Non Cryst. Solids 30 (1978) 29–36, https://doi.org/10.1016/0022-3093(78)90053-4

[9] T. Masumoto, K. Hashimoto, Chemical properties of amorphous metals, Annu. Rev. Mater. Sci. 8 (1978) 215–233, https://doi.org/10.1146/annurev.ms.08.080178.001243

[10] A. Gebert, K. Mummert, J. Eckert, L. Schultz, A. Inoue, Electrochemical investigations on the bulk glass forming Zr55Cu30Al10Ni5 alloy, Mater. Corros. Korros. 48 (1997) 293–297, https://doi.org/10.1002/maco.19970480504

[11] A. Gebert, K. Buchholz, A. Leonhard, K. Mummert, J. Eckert, L. Schultz, Investigations on the electrochemical behaviour of Zr-based bulk metallic glasses, Mater. Sci. Eng. A 267 (1999) 294–300, https://doi.org/10.1016/S0921-5093(99)00105-7

[12] A. Gebert, K. Buchholz, A.M. El-Aziz, J. Eckert, Hot water corrosion behaviour of Zr–Cu–Al–Ni bulk metallic glass, Mater. Sci. Eng. A 316 (2001) 60–65, https://doi.org/10.1016/S0921-5093(01)01248-5

[13] C.L. Qin, W. Zhang, Q.S. Zhang, K. Asami, A. Inoue, Electrochemical properties and surface analysis of Cu-Zr-Ag-Al-Nb bulk metallic glasses, J. Alloy. Compd. 483 (2009) 317–320, https://doi.org/10.1016/j.jallcom.2008.07.157

[14] Y. Gu, Z. Zheng, S. Niu, W. Ge, Y. Wang, The seawater corrosion resistance and mechanical properties of Cu 47.5Zr47.5Al5 bulk metallic glass and its composites, J. Non Cryst. Solids 380 (2013) 135–140, https://doi.org/10.1016/j.jnoncrysol.2013.08.030

[15] B. Duran, G. Bereket, Cyclic voltammetric synthesis of poly(N-methyl pyrrole) on copper and effects of polymerization parameters on corrosion performance, Ind. Eng. Chem. Res. 51 (2012) 5246–5255, https://doi.org/10.1021/ie300208c

[16] R.W. Revie, Uhlig's Corrosion Handbook: Third Edition, 2011. ⟨https://doi.org/10.1002/9780470872864⟩.

[17] M.M. Antonijević, S.M. Milić, M.B. Petrović, Films formed on copper surface in chloride media in the presence of azoles, Corros. Sci. 51 (2009) 1228–1237, https://doi.org/10.1016/j.corsci.2009.03.026

[18] Y.I. Kuznetsov, L.P. Kazansky, Physicochemical aspects of metal protection by azoles as corrosion inhibitors, Russ. Chem. Rev. 77 (2008) 219–232, https://doi.org/10.1070/rc2008v077n03abeh003753

[19] M. Finšgar, I. Milošev, Inhibition of copper corrosion by 1,2,3-benzotriazole: a review, Corros. Sci. 52 (2010) 2737–2749, https://doi.org/10.1016/j.corsci.2010.05.002

[20] I. Milošev, N. Kovačević, J. Kovač, A. Kokalj, The roles of mercapto, benzene and methyl groups in the corrosion inhibition of imidazoles on copper: I. Experimental characterization, Corros. Sci. 98 (2015) 107–118, https://doi.org/10.1016/j.corsci.2015.05.006

[21] N. Kovačević, I. Milošev, A. Kokalj, The roles of mercapto, benzene, and methyl groups in the corrosion inhibition of imidazoles on copper: II. Inhibitor-copper bonding, Corros. Sci. 98 (2015) 457–470, https://doi.org/10.1016/j.corsci.2015.05.041

[22] S. Pauly, J. Bednarik, U. Kühn, J. Eckert, Plastically deformable Cu-Zr intermetallics, Scr. Mater. 63 (2010) 336–338, https://doi.org/10.1016/j.scriptamat.2010.04.034

[23] D. Zander, U. Köster, Corrosion of amorphous and nanocrystalline Zr-based alloys, Mater. Sci. Eng. A 375–377 (2004) 53–59, https://doi.org/10.1016/j.msea.2003.10.230

[24] A. Gebert, P.F. Gostin, L. Schultz, Effect of surface finishing of a Zr-based bulk metallic glass on its corrosion behaviour, Corros. Sci. 52 (2010) 1711–1720, https://doi.org/10.1016/j.corsci.2010.01.027

[25] A. Kawashima, K. Ohmura, Y. Yokoyama, A. Inoue, The corrosion behaviour of Zr-based bulk metallic glasses in 0.5M NaCl solution, Corros. Sci. 53 (2011) 2778–2784, https://doi.org/10.1016/j.corsci.2011.05.014

[26] Y. Feng, A.H. Cai, D.W. Ding, Y. Liu, H. Wu, Q. An, H. Ning, G.J. Zhou, Y.Y. Peng, Composition design and properties of Cu–Zr–Ti bulk metallic glass composites, Mater. Chem. Phys. 232 (2019) 452–459, https://doi.org/10.1016/j.matchemphys.2019.05.030

[27] J.C. Turn, R.M. Latanision, The influence of structure on the corrosion of glassy copper-zirconium alloys, Corrosion 39 (1983) 271–279, https://doi.org/10.5006/1.3581912

[28] M. Naka, K. Hashimoto, T. Masumoto, Corrosion behavior of amorphous and crystalline Cu50Ti50 and Cu50Zr50 alloys, J. Non Cryst. Solids 30 (1978) 29–36, https://doi.org/10.1016/0022-3093(78)90053-4

[29] A. Kokalj, M. Lozinšek, B. Kapun, P. Taheri, S. Neupane, P. Losada-Pérez, C. Xie, S. Stavber, D. Crespo, F.U. Renner, A. Mol, I. Milošev, Simplistic correlations between molecular electronic properties and inhibition efficiencies: do they really exist? Corros. Sci. 179 (2021) 108856, https://doi.org/10.1016/j.corsci.2020.108856

[30] H. Okamoto, Cu-Zr (copper-zirconium), 204–204, J. Phase Equilibria Diffus. 29 (2008), https://doi.org/10.1007/s11669-008-9267-2

[31] Y. Xu, X. Liu, L. Gu, J. Wang, P. Schützendübe, Y. Huang, Y. Liu, Z. Wang, Natural oxidation of amorphous CuxZr1-x alloys, Appl. Surf. Sci. 457 (2018) 396–402, https://doi.org/10.1016/J.APSUSC.2018.06.130

[32] S. Harel, J.M. Mariot, C.F. Hague, Electronic structure at zirconia-nickel and zirconia-nickel oxide interfaces, Surf. Sci. 269–270 (1992) 1167–1172, https://doi.org/10.1016/0039-6028(92)91411-4

[33] L. Kumar, D.D. Sarma, S. Krummacher, XPS study of the room temperature surface oxidation of zirconium and its binary alloys with tin, chromium and iron, Appl. Surf. Sci. 32 (1988) 309–319, https://doi.org/10.1016/0169-4332(88)90016-5

[34] L. Young, Anodic oxide films: Part 4. - The interpretation of impedance measurements on oxide coated electrodes on niobium, Trans. Faraday Soc. 51 (1955) 1250–1260, https://doi.org/10.1039/TF9555101250

[35] L. Young, Anodic oxide films, Academic Press,, London;;New York (N.Y.), 1961.

[36] B. Tribollet, V. Vivier, M.E. Orazem, EIS technique in passivity studies: determination of the dielectric properties of passive films, Encyclopedia of Interfacial Chemistry, Elsevier, 2018, pp. 93–107, https://doi.org/10.1016/b978-0-12-409547-2.13817-x

[37] Y. Xu, L.P.H. Jeurgens, P. Schützendübe, S. Zhu, Y. Huang, Y. Liu, Z. Wang, Effect of atomic structure on preferential oxidation of alloys: amorphous versus crystalline Cu-Zr, J. Mater. Sci. Technol. 40 (2020) 128–134, https://doi.org/10.1016/j.jmst.2019.10.001

[38] A. Masuhr, T.A. Waniuk, R. Busch, W.L. Johnson, Time scales for viscous flow, atomic transport, and crystallization in the liquid and supercooled liquid states of Zr 41.2 Ti 13.8 Cu 12.5 Ni 10.0 Be 22.5, Phys. Rev. Lett. 82 (1999) 2290–2293, https://doi.org/10.1103/PhysRevLett.82.2290

[39] G.D. Bengough, R. May, Seventh report to the Corrosion Research Committee of the Institute of Metals, J. Inst. Met. 32 (1924) 90–269.

[40] G.D. Bengough, G. Jones, R. Pirret, Diagnosis od brass condenser tube corrosion, J. Inst. Met. 23 (1920) 65–137.

[41] K.F. Khaled, The inhibition of benzimidazole derivatives on corrosion of iron in 1 M HCl solutions, Electrochim. Acta 48 (2003) 2493–2503, https://doi.org/10.1016/S0013-4686(03)00291-3

[42] K.M. Ismail, Evaluation of cysteine as environmentally friendly corrosion inhibitor for copper in neutral and acidic chloride solutions, Electrochim. Acta 52 (2007) 7811–7819, https://doi.org/10.1016/j.electacta.2007.02.053

[43] P. Rodič, J. Katić, D. Korte, P. Desimone, M. Franko, S. Ceré, M. Metikoš-Huković, I. Milošev, The effect of cerium ions on the structure, porosity and electrochemical properties of Si/Zr-based hybrid sol-gel coatings deposited on aluminum, Metals 8 Basel,, 2018, p. 248, https://doi.org/10.3390/met8040248

[44] J.R. Scully, Polarization resistance method for determination of instantaneous corrosion rates, Corrosion 56 (2000) 199–217, https://doi.org/10.5006/1.3280536

[45] D.B. Miracle, The efficient cluster packing model - an atomic structural model for metallic glasses, Acta Mater. 54 (2006) 4317–4336, https://doi.org/10.1016/j.actamat.2006.06.002

[46] Y. Yang, J.F. Zeng, A. Volland, J.J. Blandin, S. Gravier, C.T. Liu, Fractal growth of the dense-packing phase in annealed metallic glass imaged by high-resolution atomic force microscopy, Acta Mater. 60 (2012) 5260–5272, https://doi.org/10.1016/j.actamat.2012.06.025

[47] A. Martínez, Bonding interactions of metal clusters [Mn (M= Cu, Ag, Au; n=1-4)] with ammonia. Are the metal clusters adequate as a model of surfaces? J. Braz. Chem. Soc. 16 (2005) 337–344, https://doi.org/10.1590/S0103-50532005000300007

[48] M. Zhou, M. Chen, L. Zhang, H. Lu, Reactions of zirconium and hafnium atoms with ammonia. Matrix infrared spectra and density functional calculations of the MNH3 and H2MNH (M = Zr and Hf) molecules, J. Phys. Chem. A. 106 (2002) 9017–9023, https://doi.org/10.1021/jp020971w